Halevi's extension of the Euler-Drude model for plasmonic systems

Gino Wegner [1,2,*] Dan-Nha Huynh [1] N. Asger Mortensen [3,4] Francesco Intravaia [1] and Kurt Busch [1,5]

[1] *Humboldt-Universität zu Berlin, Institut für Physik, AG Theoretische Optik and Photonik, 12489 Berlin, Germany*

[2] *Friedrich-Schiller-University Jena, Institute of Condensed Matter Theory and Optics, Max-Wien-Platz 1, 07743 Jena, Germany*

[3] *POLIMA – Center for Polariton-driven Light-Matter Interactions, University of Southern Denmark, Campusvej 55, DK-5230 Odense M, Denmark*

[4] *Danish Institute for Advanced Study, University of Southern Denmark, Campusvej 55, DK-5230 Odense M, Denmark*

[5] *Max-Born-Institut, 12489 Berlin, Germany*

(Received 10 November 2022; revised 28 February 2023; accepted 13 March 2023; published 24 March 2023)

The nonlocal response of plasmonic materials and nanostructures is often described within a hydrodynamic approach, which is based on the Euler-Drude equation. In this paper, we reconsider this approach within an extension proposed by Halevi [Phys. Rev. B **51**, 7497 (1995)]. After discussing the impact of this extended model on the propagation of longitudinal volume modes, we reevaluate within this framework the Mie scattering coefficients for a cylinder and the corresponding plasmon-polariton resonances. Our analysis reveals a nonlocal, collisional, and size-dependent damping term, which influences the resonances in the extinction spectrum. A transfer of the Halevi model into the time domain allows to identify a contribution to the current, which shares similarities with Cattaneo-kind diffusive-wavelike dynamics. After a comparison to other approaches commonly used in the literature, we implement the Halevi model into the discontinuous-Galerkin time-domain finite-element Maxwell solver and identify an oscillatory contribution to the current. Such an implementation of the Halevi model in time domain is of particular importance for applications in nanoplasmonics where nanogap structures and other nanoscale features have to be modeled efficiently and accurately.

DOI: 10.1103/PhysRevB.107.115425

I. INTRODUCTION

Over the last decades, the preparation of complex metallic nanostructures has experienced tremendous progress due to advances in material quality and nanostructuring techniques. Examples are dimers of spheres [1] and cylindrical wires [2], mixed wire-sphere systems [3], and bowtie antennas. The latter are connected [4] or unconnected [5], tip-to-tip nanotriangles. All such dimers (and many more conceivable structures) feature nanogaps that give rise to strong field enhancements. This characteristic can be exploited for numerous applications, which include (but are certainly not limited to) sensing via surface- and tip-enhanced Raman scattering and surface-enhanced infrared absorption spectroscopy as well as various wave-mixing processes. The performance of such devices relies on the plasmonic properties of the conduction electrons at optical frequencies. These properties can be tailored via the choice of material as well as via size and geometry [6] of the system's constituents as well as their surface preparation [7,8].

The efficient modeling of plasmonic nanostructures on both, the interpretative and predictive level requires appropriate material models. These can be distinguished by their ability to capture the relevant physics of the systems over the involved time- and lengthscales and by their propensity for a performant numerical implementation. Owing to the dispersive nature of the plasmonic material response, the latter aspect is particularly important for time-domain simulations of the Maxwell equations. One particular semiclassical model, which satisfies these requirements is often referred to as the hydrodynamic [9–12] or hydrodynamic Drude model [13–15]. While its coarseness allows for a language of just a few degrees of freedom, it nonetheless captures certain quantum effects, which become relevant in the nanometer regime. Such properties facilitate the treatment of scattering phenomena in structures with features ranging from the nanoscale to the macroscopic size. This allows for a multiscale aspect, which is accompanied by a moderate usage of computational resources. An illustrative phenomenon, which is well described by the original hydrodynamic model is the size-dependent shift of plasmonic resonances for small metallic particles [16–19].

All these attractive features of the hydrodynamic model have inspired several extensions with the aim of giving a more accurate description of the physics without substantially increasing the complexity. This endeavour is motivated by the possibility of describing new phenomena, which should be detectable in (and relevant for) experiments. For instance, in the so-called generalized nonlocal optical response (GNOR) model [18,19], the standard hydrodynamic current is supplemented by a current that follows Fick's first diffusion law, relating the diffusive current to the gradient of the (charge) density. Through the addition of this diffusive dynamics, the GNOR model is able to qualitatively describe, next to the shift, the size-dependent broadening of the plasmonic

*wegner@physik.hu-berlin.de

resonances. Another interesting extension of the hydrodynamic model was proposed by Halevi [20] on the basis of the Boltzmann-Mermin approach [21]. Within this approach it is possible to account for the different values of the hydrodynamic compressibility factor and the closely related speed of sound, which have been derived in the literature.

In this paper, we will reconsider the plasmonic response of metallic structures by direct application of Halevi's extension of the hydrodynamic model, which we refer to as the Halevi model. As we go along, we also focus on various extensions to the original hydrodynamic model and elaborate on the difficulties of a one-to-one identification with the GNOR model. We address the electromagnetic response near the surface of a finite scatterer that arises from the dynamics of (conduction) electrons within the bulk prescribed by the Halevi as well as the GNOR model. Specifically, we consider nanoscale wires as prototypical structures. In fact, nanowires are rather popular and convenient for experimental studies as they can be fabricated with excellent quality via membrane- or template-based synthesis with diameters down to about 5 nm [22]. Possible nanoscale devices that utilize plasmonic nanowires include waveguides [23,24], nanoantennas [6], and sensors [3]. Within the hydrodynamic model and under orthogonal illumination, analytical expressions for the electromagnetic fields in and around infinitely-extended straight plasmonic nanowires exist both in the quasistatic [25] and in the fully retarded [16] limit. In particular, we aim at extending the work of Ref. [16] to the Halevi model.

The paper is organized as follows. In Sec. II we briefly review the basics of the hydrodynamic Drude model and elaborate on the extension derived by Halevi. Further, we place this description into the framework of the viscoelastic model [26] in order to deepen the conceptual understanding and provide a route for future extensions. In the subsequent Sec. III, we adapt the theory developed in Ref. [16] to the Halevi model, provide a corresponding justification, and elaborate on the implications. In particular, we discuss the Halevi model's influence on mode propagation and derive the frequencies of the localized surface-plasmon-polaritons existing at the boundary of the wire. The latter reveal a nonlocality-induced damping term, which can be connected to an earlier phenomenological proposition for the reduction of the mean-free-path and resonance broadening [27,28]. In the subsequent Sec. IV we develop the time-domain formulation of the Halevi model. We explicitly show that the Halevi extension to the hydrodynamic model introduces a current that is conceptually closely related to the Cattaneo current [29], which models classical diffusion processes with finite propagation velocity. Next, in Sec. V we briefly review the GNOR-model and proceed to a detailed comparison with the Halevi model, specifically regarding the respective diffusive paradigms. We will show that, despite certain similarities, there are marked differences between the two models, which prohibit a one-to-one mapping. In Sec. VI we then proceed to numerical simulations of the scattering setup of Sec. III using the time-domain formulation of the Halevi model. We, thereby, analyze the influence of the Halevi extension on the propagation of the electric field and the mode profiles. Finally, in Sec. VII we summarize our findings and provide an outlook for future studies.

II. JUSTIFICATION OF THE HALEVI MODEL

It appears that Felix Bloch proposed and discussed the first treatment of electron dynamics by means of a hydrodynamic model [20] (see also Refs. [19,30–32] for further discussions). Back in 1933 such an approach provided an analytically amenable means to estimate the stopping power associated with the response of certain atoms [33]. Since then, the model has been rederived and extended following different paradigms. Usually the connection to conservation equations is pointed out and their specific forms are related to an equation of state. The latter may be deduced from (quantum) statistics [31,34–36]. A special case is the derivation of the equations of motion from an energy principle. Within such an approach, the equation of state follows from the choice of internal energy functional [17,30,33,37,38]. Another strategy considers already existing, semiclassical models and tries to asymptotically identify their response functions with those, which are motivated by continuum theories [20,26,38,39]. In the present paper, we follow the latter approach.

The continuum assumption lies at the heart of hydrodynamic models for describing the conduction electrons in metals: A mesoscopic perspective is adapted where the electrons form a charged fluid such that a given fluid element is (i) much larger than the actual constituents of the fluid and their mean separation and (ii) much smaller than the volume occupied by the fluid [40]. The ionic background is treated as a rigid, motionless continuum—the rigid jellium [41]—and restores overall charge neutrality. The thus introduced electron continuum may dynamically change shape and volume.

The associated dynamical quantities are the moments of a distribution function that describes the microscopic electron dynamics. Quite generally, this distribution function $f(\mathbf{r}, \mathbf{p}, t)$ represents the probability of finding at time t a representative electron with its microscopic momentum $\mathbf{p}$ in an infinitesimal volume element surrounding the position $\mathbf{r}$. This effective one-particle distribution function is obtained from the distribution function of the full N-body-electron system by integrating over the positions and microscopic momenta of the remaining $N-1$ particles. Due to the Coulomb interaction between the electrons, as well as their interaction with the ionic background, the dynamics of a m-particle distribution contains terms that couple to the $m+1$-particle distribution where $0 < m < N$. This coupled set of $N-1$ equations is referred to as the Bogoliubov-Born-Green-Kirkwood-Yvon hierarchy [34,42]. Breaking this hierarchy then facilitates the implementation of the above-mentioned method of moments. Among the truncated descriptions of one-particle distributions, a suitable equation of motion, from which the hydrodynamic equations can be deduced is the Boltzmann equation [43,44] with an electron-ion collision integral. The latter is, nowadays, usually expressed following Mermin's recipe for a charge-conserving, single-relaxation-time correction [21] and the electron Coulomb interaction is treated by a mean-field approximation. Upon expanding the distribution function of the Boltzmann-Mermin model into the moments of the microscopic momentum another hierarchy of evolution equations is obtained: Successive-order moments become coupled and the individual equations of motion represent conservation laws. A closed set of equations of motion

can be obtained through further approximations that relate a given moment to lower-order moments only. Specifically, this procedure is connected to additional approximations to the chosen coupling term of the distribution functions.

The standard hydrodynamic model considers the first- and second-order moments, charge- and momentum density, and the corresponding equations of motion ensure charge conservation and momentum balance. In the resulting evolution equations, the momentum density is often replaced by the charge current density. The omission of higher-order moments and the corresponding equations of motions is tied to the absence of heat conduction [35] and to a specific form of the stress tensor—the momentum current density tensor. The latter is given by a pressure that can solely be expressed in terms of the charge density, which, e.g., may be derived from the Thomas-Fermi theory of a degenerate electron gas [33]. The aforementioned second hierarchy is thereby terminated, producing a closed set of equations. This description provides a starting point in the sense that it incorporates quantum-statistical effects in the kinetic energy of the electronic many-body system. Eventually this leads to a nonlocal response, while it excludes certain effects such as the electrons' exchange-correlation dynamics. In a first approximation, however, this effect can be neglected at least in three-dimensional systems with sufficiently high densities of free electrons. This is motivated by the dominance of the kinetic energy contribution in such systems [45]. Different choices for the stress tensor are possible depending on the desired level of accuracy and on the particular physical system. In principle, more sophisticated models could be introduced, leaving the coupling term of momentum and energy density untouched. Then, a constitutive equation for the heat conduction could be provided as it would otherwise couple to even higher-order equations beyond the conservation of energy [35].

In the hydrodynamic formulation, the equation of motion of the charge density is dictated by the continuity equation

$$\partial_t \rho(\mathbf{r}, t) + \nabla \cdot \mathbf{J}(\mathbf{r}, t) = 0. \tag{1}$$

Due to absence of source and sink terms, the above equation stipulates that charges are neither produced nor annihilated. The conservation of the current density $\mathbf{J}$ (or, equivalently, momentum conservation) is given by the linearized Euler equation of classical fluid dynamics [40]

$$\partial_t \mathbf{J}(\mathbf{r}, t) = \epsilon_0 \omega_\mathrm{p}^2 \mathbf{E}(\mathbf{r}, t) - \beta_\mathrm{TF}^2 \nabla \rho(\mathbf{r}, t), \tag{2}$$

where we neglected the effects of magnetic fields [46]. For an electron fluid, the Thomas-Fermi pressure, arising from the Pauli exclusion principle, is responsible for the compressibility factor giving rise to the velocity $\beta_\mathrm{TF} = v_\mathrm{F}/\sqrt{3}$ with v_F the Fermi velocity [34]. In fact, the parameter β_TF may be viewed as the speed of sound in the electron continuum [47] and, accordingly, characterizes the propagation of density or pressure waves [18], which may build up in the electron continuum. The total current at position $\mathbf{r}$ is defined via the center-of-mass motion of the local fluid element induced by the total electric field $\mathbf{E}(\mathbf{r}, t)$. This field itself is in turn induced by the motion of the electron density relative to the fixed jellium background and any externally applied electric fields.

A first correction of Eq. (2) is the addition of the Drude term $-\gamma \mathbf{J}$ to the right-hand side (r.h.s.), yielding the Euler-Drude model. This additional term is actually part of the first-order moment of the single-relaxation-time approximation, discussed above. It phenomenologically describes a collection of dissipative processes that the charge carriers experience within the material. A prominent example is the hinderance in the electronic motion originating in collisions with the ionic background due to impurities or defects in the lattice or even due to the interaction with lattice vibrations (phonons). Such processes are usually added, assuming that one process does not effect the other (Matthiessen rule [44]). Further, the appearance of their cumulative collision rate γ in one of the conservation equations signifies that the associated quantity is not conserved by the collisional processes. Accordingly, this rate should only group processes, which conserve the same quantities. In our case, the collisions conserve charge by keeping Eq. (1) untouched but diminish electron momentum [26]. As Bloch points out, the Thomas-Fermi model has been applied to the static behavior of the electron continuum. From Eq. (2) we, thus, expect a quasistatic description. But such a treatment fails for typical metals at optical frequencies. As a remedy, the very same equation may be used by replacing the low-frequency value β_TF with the high-frequency value $\beta_\mathrm{HF} = \sqrt{3/5} v_\mathrm{F}$ [9,17–20,31]. Naturally, the question arises which characteristic velocity should be used, in general [20,32]. A model within the continuum approach that interpolates between the two limits has been provided by Halevi [20]. Specifically, Halevi considers the Euler-Drude model in $(\mathbf{r}, \omega)$ space and introduces a frequency-dependent velocity $\beta_\mathrm{H}(\omega)$ yielding

$$-i\omega \mathbf{J}(\mathbf{r}, \omega) = \epsilon_0 \omega_\mathrm{p}^2 \mathbf{E}(\mathbf{r}, \omega) - \beta_\mathrm{H}^2(\omega) \nabla \rho(\mathbf{r}, \omega) - \gamma \mathbf{J}(\mathbf{r}, \omega). \tag{3}$$

The longitudinal dielectric function with wavenumber k and frequency ω is derived from Eq. (3) and the Fourier transform of the continuity equation (1). A comparison between an expansion of this function and the one of the Boltzmann-Mermin model up to second order in the parameter $k v_\mathrm{F}/\omega$ allowed Halevi to obtain [20]

$$\beta_\mathrm{H}^2(\omega) = \frac{\frac{3}{5}\omega + \frac{i\gamma}{3}}{\omega + i\gamma} v_\mathrm{F}^2 = \beta_\mathrm{HF}^2 - \frac{4}{15} \frac{i\gamma}{\omega + i\gamma} v_\mathrm{F}^2. \tag{4}$$

The crossover regime is characterized by the Drude collision rate γ. Indeed, Eq. (4) interpolates between the low-frequency velocity $\beta(\omega \ll \gamma) = \beta_\mathrm{TF}$ in the collision-dominated limit and the high-frequency velocity $\beta(\omega \gg \gamma) = \beta_\mathrm{HF}$ in the field-dominated limit [20]. We refer to the system of equations (1) and (2) in the respective limits as the low- and high-frequency Euler-Drude model. For typical metals ω_p lies in the visible or ultraviolet, such that $\gamma^2 \ll \omega_\mathrm{p}^2$ and, therefore, the high-frequency value β_HF is preferred at optical frequencies $\omega \sim \omega_\mathrm{p}$. For intermediate frequencies, β_H exhibits dispersion, which Halevi relates to a phase mismatch between pressure and density fluctuations [20]. Notice that the approach followed by Halevi avoids contributions that scale as the second or higher powers of the Laplacian ∇^2, or $\nabla(\nabla\cdot)$, or other combinations of vectorial differential operators. Further, the Halevi approach guarantees local charge conservation due to

Mermin's relaxation time approximation [21]. Also in this case, however, the model does not account for any exchange-correlation effect since the high-frequency, collisionless limit of the Boltzmann-Mermin model, i.e., the Vlasov model [31], is not including them [39].

In order to deepen the physical understanding of the transition from β_{TF} to β_{HF}, we recall [39] that the Halevi model may be viewed as the longitudinal projection of the viscoelastic model derived in Ref. [26]. While Halevi's viewpoint focusses more on a formal correspondence to fluid dynamics, the viscoelastic model emphasizes elastic contributions in the high-frequency limit that are well known from the properties of solids. Accordingly, next to the compressibility of the electron continuum, which remains constant over the frequency range $\hbar\omega \ll E_{\mathrm{F}}$, where E_{F} is the Fermi energy of the metal continuum, the high-frequency limit introduces elastic shear. In contrast, the hydrodynamic limit of the viscoelastic model is determined via the same compressibility, which is augmented with a kinematic viscosity for small but finite frequency. The hydrodynamic bulk viscosity actually vanishes. This is similar to a hypothesis made by G.G. Stokes about the total pressure, which is assumed to be independent of the temporal change of the fluid density during a uniform dilatation [48]. The range of applicability of the viscoelastic model is set by the constraints [26,41]

$$k \ll 2k_{\mathrm{F}}\ , \quad \omega \gg k v_{\mathrm{F}}\ , \quad \omega, \gamma \ll E_{\mathrm{F}}/\hbar, \tag{5}$$

where k_{F} is the Fermi wave vector. Here, the first, third, and fourth inequalities facilitate the interpretation of the underlying dynamics in terms of the Boltzmann equation with collisions, where the momentum relaxes according to Mermin's recipe on the timescale $\sim 2\pi/\gamma$. The second inequality implies the transition to the viscoelastic paradigm confined by the hydrodynamic and elastic limits [41]. The formal equivalence of these limits stems from the momentum conservation equation, which can be rephrased in terms of the current density according to

$$\begin{aligned} &-\omega(\omega + i\gamma)\mathbf{J}(\mathbf{r},\omega) \\ &\quad = -i\omega\omega_{\mathrm{p}}^2\epsilon_0\mathbf{E}(\mathbf{r},\omega) + \left[\tilde{\beta}^2 - \tfrac{4}{3}i\omega\tilde{\eta}\right] \\ &\qquad \times \boldsymbol{\nabla}[\boldsymbol{\nabla}\cdot\mathbf{J}(\mathbf{r},\omega)] + i\omega\tilde{\eta}\boldsymbol{\nabla}\times\boldsymbol{\nabla}\times\mathbf{J}(\mathbf{r},\omega). \end{aligned} \tag{6}$$

Here, in the high-frequency limit, the center-of-mass velocity of an infinitesimal volume around a given position originates from the temporal change of the displacement of an infinitesimal charge element due to compression and/or elastic shear [26].

When comparing this result with the longitudinal and transverse response of the Boltzmann-Mermin model up to the second order in the wavenumber, it turns out that the velocity $\tilde{\beta}$ is just the Thomas-Fermi velocity. Further, the parameter $\tilde{\eta}(\omega)$ provides an interpolation between the velocity of elastic shear waves β_{sh} and kinematic viscosity $\eta(\omega)$ according to

$$-i\omega\tilde{\eta}(\omega) = \beta_{\mathrm{sh}}^2(\omega) - i\omega\eta(\omega). \tag{7}$$

Here, the kinematic viscosity η and the elastic shear velocity β_{sh} are real quantities given by

$$\beta_{\mathrm{sh}}^2(\omega) = \frac{\omega^2}{\omega^2+\gamma^2}\frac{v_{\mathrm{F}}^2}{5}, \quad \eta(\omega) = \frac{\gamma^2}{\omega^2+\gamma^2}\frac{v_{\mathrm{F}}^2}{5\gamma}. \tag{8}$$

Notice that similar to compression, also the shear is constrained by Pauli's exclusion principle as manifest by the appearance of the Fermi velocity in β_{sh} and η. Apart from that, the material parameters are independent of position. Thus, within the bulk, longitudinal (transverse) waves remain longitudinal (transverse). However, analogous to the theory of elasticity, at a material interface both polarisations mix [49]. This represents a key property for plasmonic nanoparticles, where the evanescent waves of surface plasmons can thus couple to bulk plasmons. For instance, transverse polarized radiation impinging onto a cylinder may excite bulk plasmons [16].

Considering that longitudinal quantities exhibit a vanishing curl, we can deduce the connection between the viscoelastic parameters and the Halevi velocity by combining Eq. (6) with the continuity equation, see Eq. (16) of Ref. [39], to yield

$$\beta_{\mathrm{H}}^2(\omega) = \beta_{\mathrm{TF}}^2 - \tfrac{4}{3}i\omega\tilde{\eta}(\omega). \tag{9}$$

Accordingly, the fact that β_{H} is a complex quantity stems from the interpolation between the fluid- and solid-like response, which, in turn, is encoded in the asymptotic expansion of the Boltzmann-Mermin model. Conceptually, the additional dispersion (as compared to the Bloch model) originates completely in viscoelasticity [39]. More precisely, within this perspective, the low-frequency, collision-dominated limit is viewed as the hydrodynamic regime and the high-frequency, collisionless limit is identified with the elastic regime [26]. Since we have for typical metals that $\omega_{\mathrm{p}} \gg \gamma$, the plasmonic response of metallic structures has to be regarded as being predominantly elastic. Therefore, and contrary to what is sometimes stated in the literature, the velocity β_{HF} is not entirely the result of the compressibility within the Thomas-Fermi model. Instead, β_{HF} also features contributions from elastic shear.

Furthermore, the elastic response at short time scales ($2\pi/\omega \ll 2\pi/\gamma$) and the viscous response at long timescales ($2\pi/\omega \gg 2\pi/\gamma$) are characteristic of highly viscous fluids [31], such as glycerin or resin [50]. As proposed by Maxwell, the deformation of such fluids due to periodic, external forces induces internal shear stress, that is damped on a certain time scale τ. As the period $2\pi/\omega$ of the external forces progresses from values much lower than τ to values much greater values than τ, the response changes its characteristics from solid like to (viscous-)liquid like [50]. In the plasmonic case τ is roughly given by $2\pi/\gamma$. Accordingly, it is the rate of Drude collisions with the ionic background that determines the extent of the solid-like response, affecting the continuum's tendency to restore its equilibrium shape. In the elastic regime, the periodic deformation is so fast that collisions cannot relax the internal stress within one period. Again, notice that the magnitude of the shear is determined by the Fermi velocity [Eqs. (7) and (8)], so that the internal stress is not only given by collisions but also tied to the Pauli principle.

Interestingly, not only the longitudinal, but also the transverse dielectric function derived from Eq. (6) is formally equivalent to a hydrodynamic dielectric function with a characteristic, squared transverse velocity $\beta_{\mathrm{T}}^2(\omega) = -i\omega\tilde{\eta}(\omega)$. In the elastic regime, we have $\beta_{\mathrm{T}} \approx \beta_{\mathrm{sh}}(\omega \gg \gamma) = v_{\mathrm{F}}/\sqrt{5}$. We emphasize this fact, since, for instance, the hydrodynamic

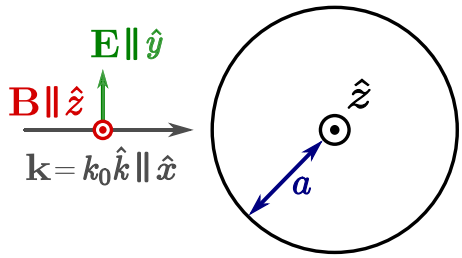

FIG. 1. Sketch of the infinitely-extended cylindrical scatterer excited normally with a plane wave propagating along the x direction and polarized normal to the rotational axis ($\hat{z}$). The electromagnetic problem effectively reduces to two dimensions.

dielectric function has been applied for the longitudinal *and* the transverse response of a metallic half-space in Ref. [51]. In the limit $\omega \sim \omega_\mathrm{p} \gg \gamma$, the values $\beta_\mathrm{L} = \beta_\mathrm{HF}$ and $\beta_\mathrm{T} = \beta_\mathrm{sh}(\omega \gg \gamma)$ have been used. Hence, the transverse and longitudinal dielectric function turn out to be high-frequency limits of the viscoelastic model—corrections towards intermediate frequencies are, thus, at hand.

The hydrodynamic perspective on the time-dependent density functional theory was recently discussed in Ref. [45] Therein, the emergence of viscous response is also mentioned. After discussing the characteristics of the Halevi model from the viewpoint of the continuum framework and its links to the viscoelastic interpretation, in the next section, we investigate the model's impact on light-matter interaction within an analytical test case.

III. EXTENDED MIE THEORY FOR A NONLOCAL, CYLINDRICAL SCATTERING PROBLEM

Analytical expressions for the quantities that describe light-matter interaction at metallic nanostructures are often tied to highly symmetric scatterers. An infinitely-long circular cylinder with radius a, homogeneous along its rotational axis and placed within vacuum is an example for such an archetypal scatterer [52]. It further represents a very good approximation to realistic cylinders with high aspect ratios [2].

Analytical formulas for the fields, given local and dispersive response within the metal, have been derived based on Mie theory [52] and have later been extended by Ruppin to allow for linear hydrodynamic response [16]. In Ruppin's work, the incident wave is injected perpendicular to the cylindrical axis and the electric field is polarized orthogonal to this axis, thus leading to an effectively two-dimensional problem (cf. Fig. 1). Specifically, as we have already mentioned in Sec. II, this setup allows for the existence and the excitation of bulk modes in the metal [16]. Following Ref. [53], Ruppin demands the absence of an infinitesimally thick surface charge density, which ultimately leads to a continuity of the radial component of the electric field. This is tied to the absence of the normal current right below the surface, similar to the hard-wall boundary condition [17,19,38]. Since, however, the tangential current may, in principle, be finite in this region, this auxiliary boundary condition (ABC) is also known as slip boundary condition [54]. Such a tangential surface current must not be mistaken with an infinitesimally thick surface current sheet, which would lead to a discontinuous, tangential magnetic field at the surface. In addition to the previous conditions, the continuity of the tangential electric field as well as the tangential (and normal) magnetic flux field is enforced.

In Ruppin's treatment, the transverse response is encoded by the Drude dielectric function given by

$$\epsilon_\mathrm{Drude}(\omega) = 1 - \frac{\omega_\mathrm{p}^2}{\omega(\omega + i\gamma)}, \tag{10}$$

which gives for the wavenumber of the internal transverse mode

$$k_\mathrm{T}^2 = k_0^2 \frac{\epsilon_\mathrm{D}(\omega)}{\epsilon_\mathrm{BG}}. \tag{11}$$

Here, $k_0 = \sqrt{\epsilon_\mathrm{BG}}\,\omega/c$ is the wavenumber of the incident wave with background dielectric function ϵ_BG. In the following, we use vacuum as the background material and thus set $\epsilon_\mathrm{BG} = 1$. The longitudinal response is given by the (high-frequency) Euler-Drude dielectric function

$$\epsilon_\mathrm{L}(k, \omega) = 1 - \frac{\omega_\mathrm{p}^2}{\omega(\omega + i\gamma) - \beta_\mathrm{HF}^2 k^2}. \tag{12}$$

The corresponding wavenumber k_L of the internal longitudinal mode derives from the implicit equation

$$\epsilon_\mathrm{L}(k_\mathrm{L}, \omega) = 0. \tag{13}$$

Completely analogous to standard Mie theory, the incident, scattered, and internal transverse portions of the electric field are expanded into solenoidal vector cylindrical harmonics. However, in the internal region an irrotational vector cylindrical harmonic is added to account for longitudinal waves. Solving for the above-described set of boundary conditions, Ruppin derives the internal longitudinal and scattered field expansions,

$$\mathbf{E}^\mathrm{L}(\mathbf{r}, \omega) = \frac{i}{k_0} \sum_{n=-\infty}^{\infty} i^n h_n \mathbf{L}_n(k_\mathrm{L}\mathbf{r}), \tag{14}$$

$$\mathbf{E}^\mathrm{S}(\mathbf{r}, \omega) = \frac{i}{k_0} \sum_{n=-\infty}^{\infty} i^n s_n \mathbf{M}_n(k_0\mathbf{r}),$$

$$\mathbf{H}^\mathrm{S}(\mathbf{r}, \omega) = \frac{1}{k_0} \sum_{n=-\infty}^{\infty} i^n s_n \mathbf{N}_n(k_0\mathbf{r}), \tag{15}$$

where $\mathbf{L}_n$, $\mathbf{M}_n$, and $\mathbf{N}_n$ are the cylindrical vector wave functions [49] and s_n are the scattering coefficients

$$s_n = -\frac{[c_n + D_n(k_\mathrm{T}a)]J_n(k_0a) - \sqrt{\epsilon_T(\omega)}J_n'(k_0a)}{[c_n + D_n(k_\mathrm{T}a)]H_n(k_0a) - \sqrt{\epsilon_T(\omega)}H_n'(k_0a)}. \tag{16}$$

Here, $J_n(x)$ and $H_n(x)$ are, respectively, the Bessel and outgoing Hankel functions of order n, while $D_n(x) = J_n'(x)/J_n(x)$. The nonlocal correction term c_n is given by

$$c_n = \frac{n^2}{k_\mathrm{L}a}[D_n(k_\mathrm{L}a)]^{-1} \frac{\epsilon_T(\omega) - 1}{k_0a\sqrt{\epsilon_T(\omega)}} \tag{17}$$

and it vanishes in the limit $\beta \to 0$, where the longitudinal nonlocality is not resolved. The expansion coefficient of the

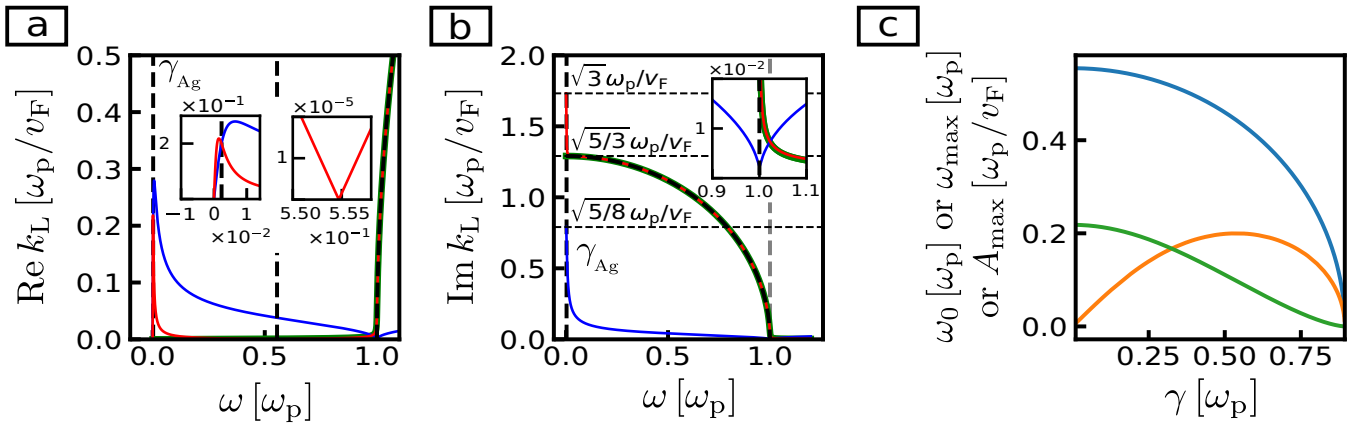

FIG. 2. Illustration of the frequency dependence of the longitudinal wavenumber k_L for the high-frequency Euler ($\gamma = 0$; black dashed line) and Euler-Drude (green solid line), the Halevi model (red solid line) and GNOR model (blue solid line) for $\gamma = 0.021$ eV (silver). For details on the latter model, see the discussion in Sec. V. The vertical dashed lines mark the damping rate and kink frequency (black) as well as the volume plasma frequency for silver (grey). (a) Real part of the wavenumber with insets showing a new local maximum (left) and kink (right). (b) Imaginary part of the wavenumber with an inset displaying how the Halevi and Euler-Drude model soften the transition at the plasma frequency. (c) Kink frequency ω_0 (blue line) as well as the frequency ω_max of the local maximum (orange line) and its amplitude $A_\mathrm{max} = \mathrm{Re}\, k_\mathrm{L}(\omega_\mathrm{max})$ (green line) in the range $0.01 < \gamma/\omega_\mathrm{p} < \sqrt{4/5}$.

internal longitudinal field reads

$$h_n = \frac{J_n(k_0 a) + s_n H_n(k_0 a)}{J_n(k_\mathrm{L} a)} \frac{ik_0 a}{\sqrt{\epsilon_T(\omega)}} \frac{c_n}{n}, \tag{18}$$

and is proportional to n. Within our definition $c_{-n} = c_n$ for $n \geqslant 1$, so that for the scattering coefficient $s_{-n} = s_n$ for $n \geqslant 1$. To prove this, the usual symmetries of the cylindrical Bessel functions and their derivatives with respect to their order are used [55].

Notice that the coefficient $c_n \propto n^2$ identically vanishes for the zeroth order such that the nonlocal and local s_0 do not differ. Accordingly, we also have $h_0 = 0$, further corroborating the absence of longitudinal effects at this order. With vacuum as the host material one has [52]

$$s_0 \underset{\sim}{\propto} (k_0 a)^4 (\sqrt{\epsilon_\mathrm{T}(\omega)} - 1), \tag{19}$$

provided that optical frequencies and radii smaller than half the plasma wavelength c/ω_p (about 10 nm for common metals) are considered. Therefore, for a spatially local response, given the aforementioned regime, $|s_0| \approx 0$. Therefore, we do not expect a significant contribution of the zeroth scattering coefficient. The poles of the $s_{\pm n}$ for $n \geqslant 1$ can be instead associated with the nth-order multipole resonances of the system. Significant contributions from the dipole ($n = 1$) as well as the quadrupole ($n = 2$) are expected in the above-mentioned regime, for which the nonlocal correction cannot be neglected.

From the discussion in Sec. II, we deduce that the Halevi model does not introduce any higher-order spatial derivatives as compared to the high-frequency Euler-Drude model. Otherwise, additional boundary conditions would have to be introduced. We can therefore directly use the wavenumbers of the Halevi model in Eqs. (16) and (17). As Ruppin points out, the longitudinal wavenumber describes the propagation of the longitudinal modes. It is then relevant to determine its features within the Halevi model and to highlight its differences with respect to that obtained with the high-frequency Euler(-Drude) model. To do so, we start with the remark that Eqs. (4), (12), and (13) directly lead to the square of the wavenumber given by

$$k_\mathrm{L}^2 = \frac{\omega(\omega + i\gamma) - \omega_\mathrm{p}^2}{\beta_\mathrm{H}(\omega)^2}, \tag{20}$$

where we substituted $\beta_\mathrm{HF} \mapsto \beta_\mathrm{H}(\omega)$, disguising some of the wavenumber's characteristics in the complex plane. The passivity of our system requires a non-negative imaginary part for k_L. By choosing the principal branch of the complex square root, the real part must remain positive.

In Fig. 2, we depict the frequency dependence of the longitudinal wavenumber for different material models of silver (see Table I for material parameters). From this, we can infer several features, which distinguish the Halevi from the Euler(-Drude) model. Specifically, below the volume plasma frequency a kink occurs [cf. right inset of Fig. 2(a)]. The associated kink frequency is derived as follows: To first order in γ/ω_p, the real part of the squared wavenumber changes

TABLE I. List of the material parameters for several metals. The Fermi velocity for Au and Ag is determined from the plasma frequency using the bare electron mass. The Drude rates of Cu, Al, and Zn were calculated using $\gamma = 2\pi/\tau$ with the relaxation time τ at 77 K taken from [44]. From these values, based on Eq. (24), the ratio Δ_1 of the nonlocal ($|\,\mathrm{Im}\,\omega_1 + \gamma/2|$) to the local damping $\gamma/2$ as well as the nonlocal damping amplitude A_1, according to Eq. (26), are inferred for $a = 1$ nm.

	ω_p [eV]	γ [eV]	v_F [10^6 $\frac{\mathrm{m}}{\mathrm{s}}$]	Δ_1	$A_1[10^{-4}]$
Ag [57]	9.149	0.021	1.408	0.025	5.657
Au [57]	8.846	0.059	1.376	0.025	16.140
Zn [44]	10.143 [58]	0.172	1.508	0.024	41.357
Al [44]	15.363 [58]	0.064	1.989	0.021	10.082
Cu [44]	7.504 [58]	0.020	1.233	0.026	6.389

sign at ω_p—being negative for frequency values below ω_p. At the same time, the imaginary part changes sign at the real frequency

$$\omega_0 = \omega_p \sqrt{\frac{4}{13} - \frac{5}{13}\frac{\gamma^2}{\omega_p^2}}, \tag{21}$$

as long as $0 < \gamma < \sqrt{4/5}\omega_p \approx 0.894\omega_p$, where $\omega_0 \approx 0.555\omega_p$ for typical metals [cf. Fig. 2(c)]. The real part of the longitudinal wavenumber, given by

$$\mathrm{Re}\, k_L(\omega) = \sqrt{\frac{\mathrm{Re}\, k_L^2(\omega) + \sqrt{\left[\mathrm{Re}\, k_L^2(\omega)\right]^2 + \left[\mathrm{Im}\, k_L^2(\omega)\right]^2}}{2}} \tag{22}$$

should exhibit a root at ω_0. At lower frequencies, we observe a local maximum [see left inset of Fig. 2(a)]. Different real parts in the different models should, in principle, lead to spatial phase differences for a given frequency. Interestingly, we observe in Fig. 2(c) that the frequency of this local maximum initially increases with γ until a value of roughly $0.2\omega_p$ is reached. Beyond this value, the frequency of the local maximum drops and vanishes at $\gamma = \sqrt{4/5}\omega_p$ along with the corresponding amplitude. Regarding the imaginary part of the longitudinal wavenumber, we notice from Fig. 2(b) that a peak occurs at low frequencies. This is due to the small velocity of the low-frequency density waves, which, in the Halevi model, reaches the Thomas-Fermi value of $\beta_{TF} = v_F/\sqrt{3} < \beta_{HF}$. Increasing the ratio γ/ω_p leads to a broadening of the peak and for the plasma frequency of bulk silver, this peak extends into the infrared frequency range. Following Ruppin, this is tantamount to a faster decay of the longitudinal modes [16] in this frequency range. Still looking at the silver curves, we deduce from the inset of Fig. 2(b) that for $\omega > \omega_p$ the decay is approximately given by the Drude damping due to the ionic background.

Now that we have determined a number of bulk features introduced by the Halevi model, we proceed to considering the surface resonances of nonlocal cylinders. In particular, we focus on the quasistatic approximation, i.e., where the incident wavelength and the skin depth are much larger than the cylinder radius. In this case, the phase of the plane wave is approximately constant across the cylinder's cross section [56]. Since we expect that the resonances are at typical wavelengths, i.e., of the order of $2\pi c/\omega_p$ (usually about hundred nanometers), the quasistatic approximation is roughly valid for radii below a few tens of nanometers. As derived in the Appendix A the leading order contribution of the nonlocality manifests itself in the dispersion relation according to

$$\omega_n \approx \omega_{sp} - \frac{i\gamma}{2} + \frac{\beta_{HF}}{2}\frac{n}{a}\left(1 - \frac{2i}{9}\frac{\gamma}{\omega_{sp}}\right), \tag{23}$$

for $n > 0$. The first three terms on the r.h.s. recover the result of the linearized Euler-Drude model regarding the nonlocal blueshift.

The imaginary part of the surface resonance frequency for the order n is given by

$$\mathrm{Im}\, \omega_n = -\frac{\gamma}{2}\left(1 + \frac{2}{9}\frac{\beta_{HF}}{\omega_{sp}}\frac{n}{a}\right). \tag{24}$$

It is proportional to the collision rate and negative, which conforms with our passivity requirement. In contrast to the well-known result for the high-frequency Euler-Drude model, the damping incorporates a nonlocal contribution. Such a feature has already been observed within the dispersion relation of the volume plasmon [20]. Therein this additional damping channel is referred to as "collision-modified Landau damping". While the plasmonic frequencies lie deep within the elastic regime, the damping term vanishes for $\gamma/\omega_p = 0$. Hence, the viscous damping, also proposed in Refs. [59,60], which contributes in the intermediate, viscoelastic regime, is essential for this damping channel to be present.

At this point we wish to emphasize that the calculations in the Appendix A are based on the limiting case $v_F n/\omega_p a \ll 1$ so that the nonlocal damping contribution is small compared to the Drude damping. In Table I, we provide the relevant parameters for a number of metals that are used in plasmonics. From this, we infer that the nonlocal damping of the dipole for cylinder radius $a = 1$ nm only contributes with about a percent of the local Drude damping, with Copper having the largest value, so that the aforementioned assumption is well justified.

Analyzing the dissipation for frequencies close to ω_n, Eq. (24) appears to suggest a description of the system in terms of a Drude dielectric function, where the damping should be amended by its nonlocal counterpart, which scales as the inverse of the cylinder radius. Such an approach would allow to avoid the intricacies that come along with the nonlocal hydrodynamic description matched by a slip boundary condition. Indeed, such an approach would yield the same expression for the imaginary part of the dispersion relation. Such an identification, however, would blur the clear conceptual distinction between bulk and surface dynamics established by the bulk dielectric function and the set of surface boundary conditions, respectively. Nevertheless, such an interpretation via a size-dependent damping rate is reminiscent of a proposition made in Refs. [27,28]. In particular, a phenomenological description of the measured extinction due to small spherical silver nanoparticles immersed in different host media is presented. The reasoning there relies on the *limited-mean-free path effects* [27,28], i.e., on the introduction of a damping process due to the interaction of the conduction electrons with the surface of the scatterer, which occurs on a lengthscale much smaller than that typical for the bulk mean-free path $\ell \sim v_F/\gamma$. In these works, the thus corrected damping rate was formally written as

$$\gamma(a) = \gamma + A\frac{v_F}{a} \tag{25}$$

and utilized within a bulk Drude dielectric function. The value of the corresponding linewidth parameter [61] A is then determined for different embedding scenarios by a fit to measured extinction data, the difference in values being motivated by a discussion of possible surface damping mechanisms. Within the Halevi model and when we assume that the cylinder is embedded in vacuum, we derive the linewidth parameter as

$$A = \frac{2n}{9}\frac{\beta_{HF}}{v_F}\frac{\gamma}{\omega_{sp}}. \tag{26}$$

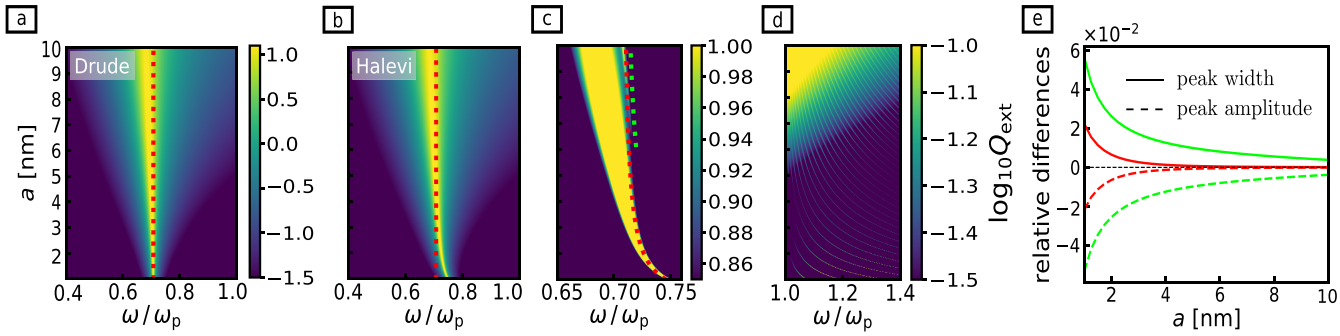

FIG. 3. Illustration of the extinction efficiencies of an infinite circular silver cylinder situated in vacuum and excited by a plane wave propagating in a plane perpendicular to the cylinder axis with polarization perpendicular to this axis. (a) Color-coded representation of the extinction efficiency as a function of radius and frequency modelled using the Drude model. The red dotted vertical line represents the local, electrostatic dipolar plasmon-polariton resonance localized at the surface of the cylinder. (b) Same as (a), but substituting the Drude with the Halevi model. The color bar is that of (a). (c) Blow-up of the dipolar and quadrupolar plasmon-polariton resonance peaks present in (b). The real part of Eq. (23) is plotted for the dipole (red dotted line) and quadrupole (green dotted line) terms. (d) Extinction efficiency for the Halevi model in the region beyond the volume plasma frequency exhibiting a nonlocal sequence of volume plasma resonances being blueshifted towards lower radii and overlapping with the dipole surface resonance at larger radii. (e) Radius dependence of the relative difference of the Halevi and the Euler-Drude model for high frequencies for the widths (solid lines) and amplitudes (dashed lines) of the dipole (red) and quadrupole (green) peak. These values have been obtained by a Lorentzian fit in the interval $0 < \omega < \omega_p$ using the Levenberg-Marquardt algorithm and only the sum element of the extinction efficiency belonging to the respective resonance. A cutoff at $\omega = \omega_p$ prevents additional fitting errors due to the excitation of bulk plasmons.

We notice that its structure is not only determined by the actual geometry and the choice of boundary condition but also depends strongly on the actual bulk response. Within the high-frequency Euler-Drude model equipped with the same boundary condition, this effect would be completely absent. While in Refs. [27,28], the phenomenological surface damping has been used to describe the dipole mode for spherical scatterers only, our analysis implies that a similar structure is to be expected for higher multipole resonances, at least for cylinders as long as $n \ll a\omega_{sp}/\beta_{HF}$. For an account of the impact of the Euler-Drude model on high-order localized plasmon-polariton resonances sustained by spheres we refer to Ref. [62]. There, e.g., the (shifted) positions of such resonances have been compared to those of a planar interface, elucidating the role of the curvature. The interpretation was further based on the actual charge distribution. A glance at Table I reveals that the value of the parameter for the dipolar resonance of silver nanowires as derived from the Halevi model in conjunction with the slip boundary condition ranges between 10^{-4} and 10^{-3}. Owing to a larger value of γ/ω_{sp}, the corresponding linewidth parameter for zinc nanowires assumes the greatest value. Experimentally, size-dependent damping has been observed for a configuration different from the one considered here, i.e., silver spheres in vacuum. For this case, a value of $A_{Ag} = 0.25$ for the dipole resonance has been determined [27]. Despite the qualitative similarities with the previous considerations, additional investigations addressing this geometry are required in order to deepen the understanding of this phenomenon. To complete our analysis of the nonlocal damping term, we briefly mention that the connection with the limited-mean-free path effects has been discussed within the GNOR model in relation to the scattering properties of metallic spheres with the very same ABC [15,18,63] (see also Refs. [64,65] for other approaches). In Sec. V, we will provide a comparison of the Halevi and this alternative model.

We conclude this section by stating that the additional damping should lead to a broadening of the quasistatic resonance peaks while, at the same time, decreasing the amplitude. This should be visible in the extinction efficiency defined as [16,62]

$$Q_{ext} = -\frac{1}{2k_0 a}\sum_{n=-\infty}^{\infty} \mathrm{Re}\, s_n, \tag{27}$$

where the s_n are defined in Eqs. (16) and (17) with the replacement $\beta_{HF} \to \beta_H(\omega)$. In Fig. 3, we depict Q_{ext} as a function of both, radius and frequency, for silver described in terms of the Drude [Fig. 3(a)] and Halevi model [Fig. 3(b)]. The results for the high-frequency Euler-Drude model are not shown because they are very similar to those of the Halevi model. Thus, the nonlocal damping introduced above only provides a small modification of the extinction efficiency. We observe that all models display a strong dipole and a weaker quadrupole resonance. The peak of the latter branches off at about 6 nm. For smaller radii, this mode is hardly discernible, since the right flank of the dipole mode is of a much larger magnitude. The nonlocality introduces bulk plasmons beyond the volume plasma frequency—a feature that is absent in the Drude model [62] and is clearly visible in Fig. 3(d). For smaller radii, the bulk and surface resonances of the Halevi model are blueshifted with decreasing radius. In order to investigate in more detail the dipolar and quadrupolar resonances, we provide in Fig. 3(c) a corresponding blow-up, where the real part of Eq. (23) is displayed with dotted lines. The dipole follows this approximation quite well up to radii of about 4 nm beyond which the approximation quickly tends to the retarded quadrupole resonance. In fact, due to

retardation the dipole resonance falls below the value $\omega_p/\sqrt{2}$ predicted within local, quasielectrostatic approximation [cf. also Eq. (23)]. This turns out to be a shortcoming of the quasistatic approximation, which relies on the smallness of the parameter $a\omega_{sp}/c$, an effect that would be pronounced for a surrounding medium with $n_{BG} > 1$, e.g., glass. For larger radii, the concomitant retardation yields a redshift of the modes, which is already visible for the Drude model. In fact, in the nonretarded limit, the Drude model would yield a complete degeneracy of all multipole resonances, such that $\omega_n \approx \omega_{sp}$, $n \geqslant 1$. The retardation-induced redshift has been phenomenologically described for small metallic spheres by employing a local material response within the framework of a self-consistent approximation of Mie theory [56]. The real part of the nonlocal and quasistatic dispersion relation, given by Eq. (23), describes a size-dependent, overall blueshift towards lower radii already present in the electrostatic limit. The shift is larger for higher multipole resonances and therefore it is more visible for the quadrupole resonance. While the blueshift scales as the dimensionless parameter $\beta_{HF}/(\omega_{sp}a)$ the redshift due to retardation scales as $\omega_{sp}a/c$ leading to a growing compensation as the radius increases. Employing the material parameters of silver given in Table I, these different scalings lead us to the following peculiarity concerning the relative weight of the effects tied to both parameters: For smaller radii $a \approx 1$ nm, we find that $\beta_{HF}/(\omega_{sp}a) \approx 0.11 > 0.03 \approx \omega_{sp}a/c$, such that the leading-order corrections due to retardation fall short of the nonlocal correction present in Eq. (23) by one order of magnitude. Accordingly, we do not expect corrections due to retardation in this equation for small radii. For larger radii $a \approx 10$ nm, the relative weight switches, since $\beta_{HF}/(\omega_{sp}a) \approx 0.01 < 0.33 \approx \omega_{sp}a/c$. Interestingly, however, according to Fig. 3(c) the overall blueshift of the quadrupole roughly compensates the red shifting for radii of about $a \approx 10$ nm, which is not true for the dipole resonance peak. Therefore, the net shift of a resonance appears to sensitively depend on the resonance order. Finally, beyond radii of 5.5 nm the right flank of the dipolar peak, which exhibits a growing asymmetry towards larger radii, increasingly overlaps with the region of bulk plasmons.

In order to quantify the effect of nonlocal damping, we fit the peaks in both, the high-frequency Euler-Drude as well as the Halevi model with Lorentzians. Afterwards, we deduce both, the width and amplitude as functions of the cylinder radius. The results are depicted in Fig. 3(e). The positive difference in widths relative to the value of the Euler-Drude model increases towards lower radii and the difference is always larger for the quadrupole mode. Both are expected from Eq. (24). The increase in width is accompanied by a decrease in amplitude, which, again, turns out to be more pronounced for the quadrupole mode. Notice, again that for increasing radii, retardation effects are pronounced. Nevertheless, the relative difference decreases in this direction.

IV. TRANSLATION INTO THE TIME DOMAIN

In Sec. III our considerations have been carried out within the frequency domain. Additional insight can be obtained from time-domain considerations. For this purpose, we consider Eqs. (3) and (4). After a few algebraic manipulations, we find

$$(-i\omega+\gamma)\mathbf{J}(\mathbf{r},\omega) = \epsilon_0\omega_p^2\mathbf{E}(\mathbf{r},\omega) - \beta_{HF}^2\nabla\rho(\mathbf{r},\omega) + \frac{4v_F^2}{15}\frac{\gamma}{\gamma-i\omega}\nabla\rho(\mathbf{r},\omega). \tag{28}$$

From our previous discussions, we recall that the Halevi model introduces additional dispersion in the nonlocal gradient term of the high-frequency Euler-Drude equation, which leads to the last term on the r.h.s. of Eq. (28). In order to incorporate dispersive response into a time-domain numerical framework, the technique of auxiliary differential equation (ADE) is often applied [66]. In our specific case, we equate the last term of Eq. (28) with a current $\mathbf{J}_D$ multiplied by the negative damping rate $-\gamma$. Performing an inverse Fourier transform to the time-domain yields the ADE

$$\partial_t\mathbf{J}_D(\mathbf{r},t) + \gamma\mathbf{J}_D(\mathbf{r},t) = -\frac{4v_F^2}{15}\nabla\rho(\mathbf{r},t), \tag{29}$$

which, apart from the temporal-derivative term on the left-hand side (l.h.s.), is reminiscent of Fick's first law, describing an ordinary diffusion current. Equation (28) can then be rephrased in the time domain as

$$\partial_t\mathbf{J}(\mathbf{r},t) = \epsilon_0\omega_p^2\mathbf{E}(\mathbf{r},t) - \beta_{HF}^2\nabla\rho(\mathbf{r},t) - \gamma[\mathbf{J}(\mathbf{r},t)+\mathbf{J}_D(\mathbf{r},t)]. \tag{30}$$

In order to clarify the origin of the auxiliary current, we consider the viscoelastic counterpart of Eq. (28). It can be derived from Eq. (6) by applying the continuity equation as well as the Gauß-Maxwell law and considering the longitudinal current only. The identification with the Halevi velocity is then mediated by Eq. (9), which can be recast into

$$\beta_H^2(\omega) = \beta_{HF}^2 + \frac{4}{3}\left[-i\omega\tilde{\eta}(\omega) - \frac{v_F^2}{5}\right]. \tag{31}$$

The squared velocity $v_F^2/5 = -i\omega\tilde{\eta}(\omega)|_{\omega\gg\gamma}$ corresponds to purely elastic waves and serves to restore the Thomas-Fermi velocity in the hydrodynamic limit. A comparison of Eq. (31) with the prefactors of the density-gradient terms in Eq. (28) eventually allows for an identification of the additional dispersion with viscoelastic shear, encoded in $\tilde{\eta}$. As visible in the second term on the r.h.s. of Eq. (6), $\tilde{\eta}$ enters there with a numerical prefactor of 4/3. Multiplying the latter with $v_F^2/5$, the squared diffusive velocity $v_D^2 = 4v_F^2/15$ in Eq. (29) is recovered.

While the dynamics of $\mathbf{J}$ is coupled directly to that of $\mathbf{J}_D$ [see Eq. (30)], the dynamics of the current $\mathbf{J}_D$ is indirectly related to $\mathbf{J}$ via the longitudinal stress $\nabla\rho(\mathbf{r},t)$ emerging in Eq. (29). We can obtain insight into the modified dynamics, introduced via the auxiliary current, by inspecting the induced charge density. For this reason, we introduce the decomposition

$$\rho = \tilde{\rho} + \rho_D. \tag{32}$$

Using Eq. (32) in the continuity equation, we obtain $\nabla\cdot\mathbf{J}_D = -\partial_t\rho_D$ and rephrase Eq. (29) as

$$\partial_t^2\rho_D + \gamma\partial_t\rho_D - v_D^2\triangle\rho_D = v_D^2\triangle\tilde{\rho}. \tag{33}$$

Interestingly, if the r.h.s. of Eq. (33) was zero the Cattaneo equation would be obtained [29]. Indeed, back in 1948, Cattaneo modified the ordinary diffusion current of a classical substance, given by Fick's first law, by employing a relaxation-time approach. This enforces a finite propagation velocity of the classically diffusing quantity [29]. Quantities that obey this type of equation perform a hybrid diffusive-wavelike propagation [49,67]. Which propagation paradigm dominates, depends on the relative temporal change of the respective quantity [67] and in our case it can be assessed through

$$f_{\mathrm{D}} = \left| \frac{\partial_t \rho_{\mathrm{D}}}{\gamma \rho_{\mathrm{D}}} \right|. \tag{34}$$

For $f_{\mathrm{D}} \gg 1$, the l.h.s. of Eq. (33) describes a wavelike transport in the collision-less regime, while for $f_{\mathrm{D}} \ll 1$ one has a diffusive transport in the collision-dominated regime. Accordingly, close to the collisionless regime, a small diffusive contribution obstructs a purely wavelike motion [49]. Notice, however, that differently from the Cattaneo equation our hybrid propagation is modulated by the dynamics of $\tilde{\rho}$ in the r.h.s. of Eq. (33).

Actually, both types of propagation are also found for the total induced charge. In order to facilitate the discussion, we introduce the rate f similar to Eq. (34), but in terms of ρ. Considering Eqs. (29) and (30) in conjunction with the Gauß-Maxwell law and the continuity equation yields

$$-\omega_{\mathrm{p}}^2 \rho = \left(\gamma \partial_t - \beta_{\mathrm{TF}}^2 \nabla^2\right)\rho \tag{35}$$

in the hydrodynamic ($f, f_{\mathrm{D}} \ll 1$) and

$$-\omega_{\mathrm{p}}^2 \rho = \left(\partial_t^2 - \beta_{\mathrm{HF}}^2 \nabla^2\right)\rho \tag{36}$$

in the elastic regime ($f, f_{\mathrm{D}} \gg 1$). Accordingly, in these regimes the conduction electrons exhibit diffusive and wavelike transport, respectively, with a propagation velocity that changes from β_{TF} to β_{HF}. This is linked to the insight that the bare Euler-Drude model yields a Cattaneo-type differential equation for the totally induced charge. However, the Cattaneo-type dynamics of the Euler-Drude model is modulated by the Coulomb interaction, which introduces a restoring force that keeps the electrons within the metal [see, for instance, the l.h.s. of Eqs. (35) and (36) in the respective asymptotic]. Incidentally, the restoring term originates in the electric field that enters Eq. (28). Since screened dielectric functions are constructed as those functions, which connect the current not only to some external but also to the internal field, we find that according to Halevi's extension

$$\epsilon_{\mathrm{H}}(k,\omega) = 1 - \frac{\omega_{\mathrm{p}}^2}{\omega(\omega + i\gamma) - \beta_{\mathrm{HF}}^2 k^2 + \gamma v_{\mathrm{D}}^2 k^2/(\gamma - i\omega)}. \tag{37}$$

The restoring term, proportional to ω_{p}^2, only enters through the numerator of the second term on the r.h.s. of Eq. (37). In the hydrodynamic regime, the pole of this very term turns purely diffusive, i.e., $\omega = -i(\beta_{\mathrm{TF}}^2/\gamma)k^2$, and becomes purely wavelike in the elastic regime, i.e., $\omega^2 = \beta_{\mathrm{HF}}^2 k^2$.

Finally, it is opportune to remark that the quantum-mechanical nature of the conduction electrons enters the equations of motion solely via the characteristic velocities β, which are all proportional to the Fermi velocity. Apart from this, these equations are similar to those of classical material dynamics. This can be understood by reformulating the fourth condition of the viscoelastic model, [see Eq. (5)] to

$$\ell \sim v_{\mathrm{F}}/\gamma \gg 1/k_{\mathrm{F}} \sim \lambda_{\mathrm{F}}. \tag{38}$$

As a result, the (bulk) mean-free-path ℓ is much larger than the Fermi wavelength λ_{F} within the viscoelastic model. Hence, a representative electron conducts a random walk in which successive collisional events are independent of each other and quantum interference effects are absent [41].

V. COMPARISON WITH THE GNOR MODEL

In the previous Sec. IV, we have shown that the Halevi model coherently extends the low- and the high-frequency Euler-Drude model via an additional current that shares some similarities with a diffusive current according to Fick's first law but also a closer connection with the Cattaneo equation. An extension of the Euler-Drude model due to diffusive dynamics is also a key element of the GNOR model [18]. Therefore, it is worthwhile to discuss similarities and differences of the GNOR and the Halevi model.

In Refs. [15,18,19,68] a generalized formal approach to nonlocality within linear response theory was discussed. Given a position $\mathbf{r}$ within the electron continuum, the influence of nonlocal processes is limited to a neighborhood with an extent that is usually smaller than the length scale of variation of the electric field. Within the constitutive equations, this allows for a Taylor expansion of the field of the electron continuum where each term corresponds to a certain order of nonlocality. For a homogeneous, isotropic medium with local response described by the Drude model, the leading-order nonlocal current density is then given by

$$-i\omega \mathbf{J}(\mathbf{r},\omega) = \epsilon_0 \omega_{\mathrm{p}}^2 \mathbf{E}(\mathbf{r},\omega) - \gamma \mathbf{J}(\mathbf{r},\omega) - \nu^2 \nabla[\epsilon_0 \nabla \cdot \mathbf{E}(\mathbf{r},\omega)]. \tag{39}$$

The last term on the r.h.s. lumps together the effects of the considered order of nonlocality that extends the local Drude response. As remarked in Ref. [19], the nonlocality manifests itself in the longitudinal current response. Since it has been pointed out that surface-plasmon-polaritons are affected not only by the longitudinal response [68], we add that the transverse nonlocality of the viscoelastic model, Eq. (6), serves as a plausible amendment.

Eventually, in order to construct the GNOR model, first the center-of-mass current $\rho_0 \mathbf{v}$ is defined to fulfill the high-frequency Euler-Drude model. The total current is then defined by the sum of the latter and a diffusive current [18,19,68], such that

$$\mathbf{J}(\mathbf{r},\omega) = \rho_0 \mathbf{v}(\mathbf{r},\omega) - D\nabla\rho(\mathbf{r},\omega). \tag{40}$$

Accordingly, the diffusion is basically introduced by hand, following Fick's first law [29,68], given a diffusion constant D. In order to prohibit the buildup of charges, this constant has to be positive. Within the definition of Eq. (40), it can then be shown that the ν^2 coefficient in Eq. (39) takes the form

$$\nu^2 = \beta_{\mathrm{HF}}^2 + D(\gamma - i\omega). \tag{41}$$

In the GNOR model, this expression represents the counterpart of Halevi's interpolation formula defined in Eqs. (4) and (31). Both models include the high-frequency Euler-Drude model, which introduces a nonlocal process characterized by the length scale $\ell_\beta = \beta_{\mathrm{HF}}/\omega$. Further, the GNOR and the Halevi model, Eqs. (41) and (31), respectively, provide an extension of β_{HF} to complex-valued velocities. In the original GNOR model, the diffusion constant is estimated via $D \sim v_{\mathrm{F}}^2/\gamma$ [18], yielding a diffusive length scale $\ell_{\mathrm{D}} = \sqrt{D/\omega} \sim v_{\mathrm{F}}/\sqrt{\gamma\omega_{\mathrm{p}}}$, which we have evaluated at the plasma frequency. Therefore, for good conductors ($\gamma/\omega_{\mathrm{p}} \ll 1$), this diffusive scale is much larger than $\ell_\beta \sim \ell_{\mathrm{D}}\sqrt{\gamma/\omega_{\mathrm{p}}}$. In contrast, within the Halevi model ℓ_β is larger than the corresponding diffusive length scale, which can be defined from Eq. (4), i.e., $\ell_{\mathrm{D}}^{\mathrm{Hal}} \sim \sqrt{\gamma/\omega_{\mathrm{p}}}(v_{\mathrm{F}}/\omega_{\mathrm{p}}) \sim \ell_\beta\sqrt{\gamma/\omega_{\mathrm{p}}}$. The mismatch in the frequency dependence of each extension to β_{HF} has also been pointed out in Ref. [60].

Within the GNOR model, the auxiliary differential equation for the additional current reads

$$\gamma\mathbf{J}_{\mathrm{GNOR}}(\mathbf{r},\omega) = \left[v^2 - \beta_{\mathrm{HF}}^2\right]\nabla\rho(\mathbf{r},\omega), \tag{42}$$

where we isolated the part proportional to β_{HF} stemming from the Euler-Drude model. Upon inserting Eq. (41) as well as the continuity equation, where the total current now obeys Eq. (40) per construction, we find

$$\gamma\mathbf{J}_{\mathrm{GNOR}}(\mathbf{r},\omega) = D\gamma\nabla\rho(\mathbf{r},\omega) - D\nabla[\nabla\cdot\mathbf{J}(\mathbf{r},\omega)]. \tag{43}$$

The dynamics of the total current within the GNOR model is then given by

$$-i\omega\mathbf{J}(\mathbf{r},\omega) = \epsilon_0\omega_{\mathrm{p}}^2\mathbf{E}(\mathbf{r},\omega) - \gamma\mathbf{J}(\mathbf{r},\omega) - \left(\beta_{\mathrm{HF}}^2 + D\gamma\right) \times \nabla\rho(\mathbf{r},\omega) + D\nabla[\nabla\cdot\mathbf{J}(\mathbf{r},\omega)]. \tag{44}$$

As a result, we see that the first term on the r.h.s. of Eq. (43) adds to the density gradient term of the high-frequency Euler-Drude equation. Beyond that the second term on the r.h.s. of Eq. (43) formally reproduces the longitudinal shear contribution of Eq. (6). The corresponding coefficient has to be positive, which is consistent with $D > 0$. Let us now utilize the frequency-dependent (real-valued) diffusion constant deduced in Ref. [19] by equating the imaginary parts of Eqs. (41) and (4) given by

$$D = \frac{v_{\mathrm{D}}^2}{\gamma}\frac{\gamma^2}{\omega^2+\gamma^2}. \tag{45}$$

We see that the prefactor of the density gradient term of Eq. (44) gives the characteristic velocity β_{HF}^2 in the high-frequency regime and $\beta_{\mathrm{HF}}^2 + v_{\mathrm{D}}^2 > \beta_{\mathrm{TF}}^2$ in the low-frequency regime. This means that the characteristic speed predicted by the GNOR model at low frequency is not in agreement with the Thomas-Fermi theory. This results from the fact that $D(\omega \gg \gamma) \sim \gamma/\omega^2$ and $D(\omega \ll \gamma) \sim 1/\gamma$, which is not the case in the Halevi model. Beyond that, by equating the real parts of Eqs. (41) and (4), we find the negative of the r.h.s. of Eq. (45) if we assume a real-valued diffusion constant.

Another difference between the GNOR and the Halevi model arises when we derive the counterpart of Eq. (40) for the Halevi model. For this purpose, we consider Eq. (28) and define the total current as

$$\mathbf{J}(\mathbf{r},\omega) = \rho_0\mathbf{v}(\mathbf{r},\omega) + \mathbf{J}_{\mathrm{H}}(\mathbf{r},\omega). \tag{46}$$

Trying to restore the high-frequency Drude-Euler equation for $\rho_0\mathbf{v}$, we require the equivalence between $\mathbf{J}_{\mathrm{H}}(\mathbf{r},\omega)$ and the residual terms and obtain

$$\mathbf{J}_{\mathrm{H}}(\mathbf{r},\omega) = -\frac{v_{\mathrm{D}}^2}{\gamma}\frac{\gamma^2}{(\omega+i\gamma)^2}\nabla\rho(\mathbf{r},\omega). \tag{47}$$

As one should expect from our comments on the Cattaneo-like dynamics involved in the Halevi approach, the dynamics of this additional current follows a non-Fickian diffusion. The difference originates in the way how local equilibrium is implemented in the Mermin approach. To yield equivalence with the Ansatz in Eq. (40), the diffusion constant does not only have to be frequency dependent, but also complex valued.

The particular choice of diffusive paradigm also influences the longitudinal wavenumber. Therefore, we added the results of the GNOR model to Figs. 2(a) and 2(b), using the approximation $D \approx \frac{v_{\mathrm{F}}^2}{\gamma}$ that has been suggested in Ref. [18]. First, the real part exhibits a low-frequency local maximum, just as the Halevi model. However, there is no additional kink root below the plasma frequency. Further, beyond the plasma frequency the high-frequency Euler(-Drude)-model is not followed as closely. Considering the imaginary part, the amplitude of the low-frequency maximum is smaller than in the high-frequency Euler-Drude model as well as the Halevi model, owing to the larger velocity $\sqrt{\beta_{\mathrm{HF}}^2 + D\gamma} > \beta_{\mathrm{HF}}, \beta_{\mathrm{TF}}$. This larger velocity is also tied to a larger blueshift for resonances that potentially occur within this frequency regime in nano-objects when considering a hard-wall boundary condition. A similar observation has been made in Ref. [63]. Further, for frequencies beyond the volume plasma frequency, the GNOR model does not follow the high-frequency Euler-Drude model as closely as does the Halevi model. Specifically, the imaginary part increases in the GNOR-model instead of decreasing in the Euler-Drude and the Halevi model.

We deduce that a direct identification of both diffusive extensions of the high-frequency Euler-Drude model has to be exercised with caution although these models share certain qualitative similarities. Interestingly, $\mathbf{J}_{\mathrm{D}}$, when added to the shear-corrected pressure term ($\propto \beta_{\mathrm{HF}}^2$) yields a viscoelastic single-relaxation-time approximation of the diffusion current derived in Eq. (31) of Ref. [69]. In this reference, a total current is derived, which is close to Eq. (40), provided a real-valued diffusion constant. However, the derivation is confined to a steady-state case. The diffusion is related to the inhomogeneity of the Thomas-Fermi pressure and, therefore, $D\gamma = v_{\mathrm{F}}^2/3$, which provides the nonlocal correction to Ohm's law. This correction is required to demonstrate that within a metal a vanishing total current does not yield a vanishing electric field (as otherwise a complete screening of charges would consequently appear [69]).

Recently, it has been reported that the GNOR model leaves the scope of the (bulk) Boltzmann(-Mermin) model by introducing high-frequency (optical) diffusion [15]. Further, a microscopic justification of the diffusive extension inherent in the GNOR model has been proposed by resorting to surface response functions that employ the Feibelman d

parameter [15,63,64]. Interestingly, the Halevi model provides an alternative unifying description of the size-dependent frequency shift and broadening of plasmonic resonances in nanometer-structured metals, which stays within the scope of the Boltzmann-Mermin model. As a result, the Halevi model is firmly rooted in bulk arguments before applying any boundary conditions. However, owing to the different scaling with the ratio γ/ω_p (given a frequency-independent D), the nonlocal damping of the Halevi model is smaller in amplitude relative to the GNOR model.

Finally, notice that Ref. [63] only considers the Boltzmann equation without the Mermin correction while the latter has been mentioned in one of the original publications on the GNOR model in Ref. [19]. Actually, in Ref. [43], the Mermin correction has been linked to an additional, diffusive current. We stress this fact, since the Mermin-Ansatz for the single-relaxation-time approximation introduces an additional term, which prohibits the occurrence of a charge sink in the continuity equation (see Refs. [8,21]).

VI. TEMPORAL EVOLUTION OF FIELDS IN THE HALEVI MODEL

Equations (1), (29), and (30) together with the slip and Maxwell's boundary conditions determine the complete system of equations for the description of plasmonic resonances within the Halevi model.

In order to solve the Maxwell equations with this material model for an arbitrary geometry of a scatterer, we implement the time-domain version of the Halevi model via ADEs (see Sec. IV) into our home-made discontinuous Galerkin time-domain (DGTD) approach [66]. The latter is a finite-element method that is specifically designed to solve equations in conservation form and we have utilized the algorithm in nodal form developed by Hesthaven and Warburton [70]. We employ third-order Lagrange polynomials as basis functions and confirm that fourth-order polynomials give, basically, the same results. Further, within the DGTD approach a numerical flux is introduced in order to couple adjacent elements. We utilize a pure upwind flux for the Maxwell equations [66,70] and employ for Eqs. (1) and (30) the Lax-Friedrichs flux [70]. Finally, we solve the ADE, Eq. (29), using a central flux. The resulting DGTD spatial discretization yields a set of ordinary differential equations of first order in time, which we solve via a fourth-order Low-Storage Runge-Kutta method with 14 stages [71]. The Drude and Euler-Drude model have also been implemented within DGTD and for details, we refer to Refs. [66] and [72], respectively.

For our subsequent simulations, we consider a cylindrical silver wire of radius 10 nm (see Table I for the material parameters) immersed in vacuum. The wire is illuminated by an electromagnetic plane wave with wave vector and electric field normal to the cylinder axis, i.e., identical to the analytical case of Sec. III (see also Fig. 1 for an illustration of the setup). The exciting pulse is centered around $\omega_0 = 7.4$ eV (which is roughly 0.8 times the plasma frequency) and has a Gaussian envelope with a FWHM of 1.57 fs. This pulse is injected into the system using the total-field/scattered-field (TF/SF) technique [66]. Since the problem effectively reduces to two dimensions, the TF/SF contour is chosen to be a square with edge length 40 nm centered on the cylinder axis. The pulse is launched from the left edge of the TF/SF contour such that the maximum there occurs at $t_0 = 4.67$ fs. The scattered field box is bounded by the TF/SF contour and a centered square of edge length 440 nm. To prevent unphysical back reflexions, we surround the entire physical domain with perfectly matched layers and apply Silver-Müller boundary conditions at the outer boundary given by a centered square with edge length 1.04 μm (see Fig. 8 for an illustrative mesh). The corresponding mesh is generated using Gmsh [73]. In order to adequately resolve the cylindrical material interface, we utilize a minimal (maximal) insphere radius of 0.04 nm (0.32 nm) for the finite elements near this interface—each element being of triangular shape. For further details on the convergence characteristics and computational resources we refer to the Appendices B and C.

In Sec. II, we have elaborated on the Halevi model as an extension of the high-frequency Euler-Drude model. Here, we proceed to perform a direct comparison of the numerical results for the two approaches and focus on the relative difference of the spatiotemporal electric field distributions according to

$$\Delta E_i(\mathbf{r},t) = \frac{E_i^{\mathrm{linHd}}(\mathbf{r},t) - E_i^{\mathrm{Hal}}(\mathbf{r},t)}{\max_{(\mathbf{r},t)} E_i^{\mathrm{linHd}}(\mathbf{r},t)}, \tag{48}$$

where $i \in \{x, y\}$, i.e., for the x and y component of the electric field. We would like to recall that our excitation pulse propagates along the x axis and is polarized along the y axis.

From Fig. 4, we infer that the x and y components exhibit differences in amplitude, which at $t \approx 4.67$ fs is most significant at the surface. As the pulse progresses, the relative differences assume the form of spatially confined oscillations close to the surface at $t \approx 6.34$ fs. Around this time, the left flank of the pulse leaves the cylinder. Around $t \approx 13.68$ fs, the oscillations have traveled about half the way to the cylinder's center and reach the center around $t \approx 20.68$ fs. Subsequently, the oscillations start to disperse across the entire cross section of the cylinder and, ultimately, become damped out. We provide the last time frame at $t \approx 46.03$ fs in order to make visible that the oscillatory pattern has distributed over the cylindrical cross section. Incidentally, the relative difference at this time instance is reminiscent of the mode picture of hydrodynamic bulk plasmons [72]. As such, the oscillations corresponding to the y component posses, e.g., a mirror symmetry with respect to the xz plane and are mapped onto themselves by a rotation of 180 degree around the cylinder axis. The oscillations within the x component, however, are mapped onto themselves, e.g., by a 90 degree rotation followed by mirroring at the yz plane. These symmetries are also present at the other time instances. Nonetheless, the differences in the field distributions are rather weak.

In Sec. IV, we have shown that the dispersion of the Halevi model [as compared to the high-frequency Euler-Drude model, Eq. (28)] translates into an additional current that follows Eq. (29). Accordingly, we expect that the difference in the electric field is tied to the spatiotemporal evolution of this additional current. Consequently, in Fig. 5 we display the x and y component of the additional current $\mathbf{J}_\mathrm{D}$ at the same time instances where we depicted the field differences in

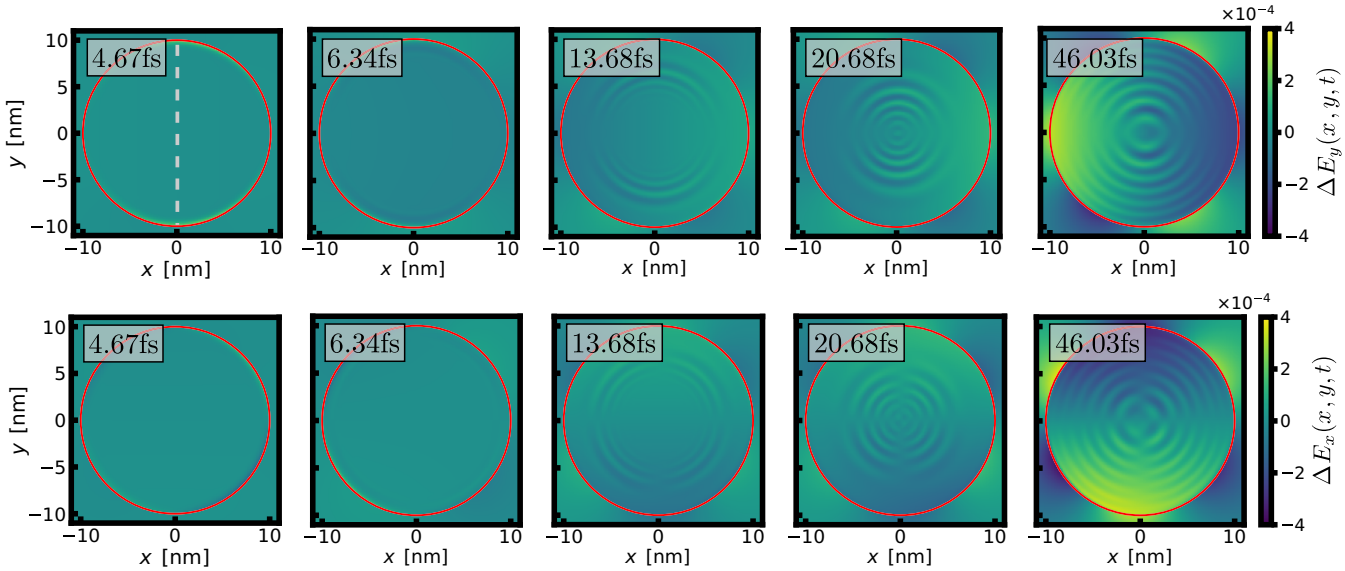

FIG. 4. Illustration of the time evolution of the relative difference of E_y (upper row) and E_x (lower row) given by Eq. (48) between the Halevi and high-frequency Euler-Drude model across the horizontal cross section of a cylindrical scatterer situated in vacuum. The cylinder has a radius of 10 nm and is made of silver with material parameters according to Table I (see also Fig. 1 for the scattering setup). Spatially confined field oscillations build up and propagate towards the center until they eventually spread across the entire disk. The vertical dashed line in the upper row marks the line considered in Fig. 6.

Fig. 4. We observe that, at all time instances, both components concentrate the maximal amplitude at the surface of the cylinder. However, a small contribution is given by the spatially confined oscillations, which propagate in essentially the same way as the relative difference in the field components, also respecting the afore-discussed symmetry properties.

In order to determine how fast the oscillations in the relative field difference propagate into the scatterer, we consider a cut through the cylinder center as indicated in Fig. 4. Given the pulsed nature of our excitation, these oscillations build up and assume the form of wave packets—due to symmetry one in each half of the cut. In Fig. 6(a) we provide an illustrative time frame. To highlight the spatial confinement, we determine the interpolative (upper and lower) envelope. Specifically, we sample the maxima and minima and perform corresponding cubic spline fits [74]. This approach works well for positions away from the surface but experiences some problems near the surface where the boundary conditions obstruct the formation of well-developed wave packets. From the global extrema of the upper and lower envelopes of, e.g., the lower wave packet, we can deduce the movement of the wave packets, which ultimately yields two

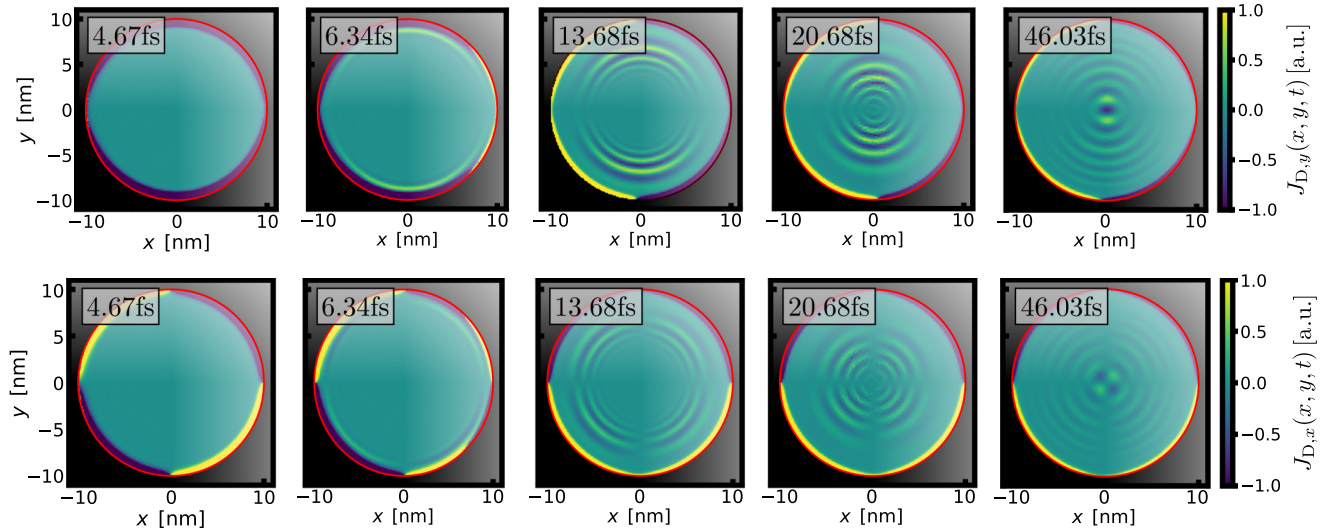

FIG. 5. Illustration of the time evolution of the current components $J_{\mathrm{D},y}$ (upper row) and $J_{\mathrm{D},x}$ (lower row) of the auxiliary current [Eq. (29)] within the horizontal cross section of a silver cylinder (radius $a = 10$ nm, see Fig. 1 for the general scattering setup). Starting from the surface region an oscillatory contribution propagates towards the cylinder's center and finally extends across the entire cross section.

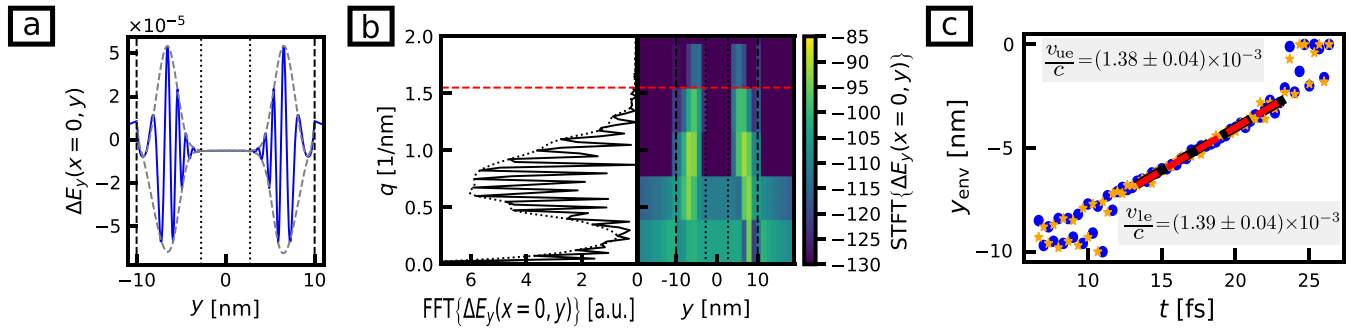

FIG. 6. Snapshot of the relative difference of E_y given by Eq. (48) between the high-frequency Euler-Drude and the Halevi model at time $t \approx 13.68$ fs along a vertical through the cylinder, as outlined by the dashed line in Fig. 4. (a) Relative difference in E_y, displaying two wave packets. (b) Onesided, spatial FFT of the signal of (a) as function of spatial frequency q (left part), as well as a spectrogram exhibiting the short-time-Fourier-transform (STFT) of the signal in panel (a) using a Hamming window (right part). Both plots of (b) feature the same y axis. The spatial frequency resolution of the spectrogram is chosen as roughly 1 nm^{-1} to bring out the positive chirp towards the center within the two wave packets of panel (a). The sampling rate of roughly 1 nm^{-1} yields a Nyquist limit of $q_{\mathrm{max}} \approx 5$ nm^{-1}. The color bar of the spectrogram is truncated to yield a better contrast in the dominant spatial frequency range of roughly $q \in [0.25, 1.5]$ nm^{-1}—the upper bound being marked by a horizontal dashed line. (c) Position y_{env} of the global maximum (blue dots) and global minimum (orange stars) of the left wave packet [as exemplified in (a) for $t \approx 13.68$ fs] as a function of time. A linear fit is provided yielding estimates for the upper envelope (ue) and lower envelope (le) group velocity.

estimates of the corresponding group velocity. For instance, we observe in Fig. 4(c) that the extrema lie close to each other from about $t \approx 12.03$ fs (at which time a nice wave packet has build up) up to about $t \approx 23.05$ fs where the two wave packets have merged. From a linear regression, we obtain the velocities $v_{\mathrm{ue}}/c = 1.38 \times 10^{-3}$ and $v_{\mathrm{le}}/c = 1.39 \times 10^{-3}$ (where c is the vacuum speed of light) for the upper and lower envelope, respectively. This is a rather interesting result, since these velocities are considerably smaller than all velocity scales that we have discussed so far. In fact, the values are closest to the elastic shear velocity $v_{\mathrm{F}}/\sqrt{5}$.

Further, within the pulse the spatial frequency experiences a chirp. Therefore, we provide in Fig. 4(b) the one-sided Fourier transform of this signal. While this provides an overview of the relevant frequency contributions it lacks the desired spatial resolution. Therefore, we also provide in Fig. 4(b) the corresponding spectrogram. Although the minimal spatial resolution of the spectrogram corresponds to about 0.1 nm, the inverse scaling between spatial frequency and spatial resolution forces us to fix the spatial resolution to about 1 nm. Despite its coarseness, this resolution allows us to elaborate on the positive spatial chirp (towards the cylinder center) within each wave packet. Specifically, we find that the highest available frequencies are tied to the region, where the wave packets are located and, in this region, they increase towards the center.

We conclude our survey by calculating the modal distributions for the dipolar and quadrupolar resonance for both, the Halevi and the high-frequency Euler-Drude model from our time-domain simulations via an on-the-fly Fourier transform. In Fig. 7 we depict the real part of the electric field distributions at these resonances for the Halevi model and the difference of these field distributions to the results of the high-frequency Euler-Drude model. In addition, we normalize the difference to the largest value obtained within the Euler-Drude model at the respective frequency in order to bring out better the deviations between the results. First, we observe that these modal patterns within the Halevi model are compatible with the symmetry classification of the Euler-Drude model [14]. Further, the (real-parts) of the field amplitudes in the Halevi model are enhanced. Specifically, for the dipole resonance we obtain an enhancement in the vicinity of the surface with a fourfold rotation symmetry for the x and y component of the electric field. For the quadrupolar resonance, the differences inside the scatterer are more inhomogeneous. Overall, the field enhancement is relatively small.

VII. CONCLUSIONS AND OUTLOOK

To summarize, we have analyzed the physical properties of the Halevi model for plasmonic materials. In particular, we have identified the Halevi model as an extension of the Euler-Drude model and have established its relation to the viscoelastic model by way of spectral as well as spatiotemporal investigations of different aspects of plasmonic light-matter interaction. We have further applied the Halevi model to Ruppin's hydrodynamic approach of Mie theory for cylinders and determined the quasistatic plasmon-polariton resonances. Thereby we have revealed a damping term, which exhibits formal similarities to the collision-modified Landau-damping previously discussed by Halevi. In turn, this might lead to a physical justification of an earlier phenomenological description of limited-mean-free path effects of dipole surface modes and we have shown how this damping term also affects higher-order plasmon resonances. For an experimental comparison, the corresponding linewidth values and the induced changes were calculated for cylindrical nanowires. The viscous shear-extension within the Halevi model eventually has lead to nonlocal surface damping. Further, the Halevi extension led to an increase in the relative difference of the width of surface dipolar and quadrupolar extinction peaks for cylinder radii in the range of 1 to 10 nm, where, generally, the effect is larger for the quadrupolar resonance.

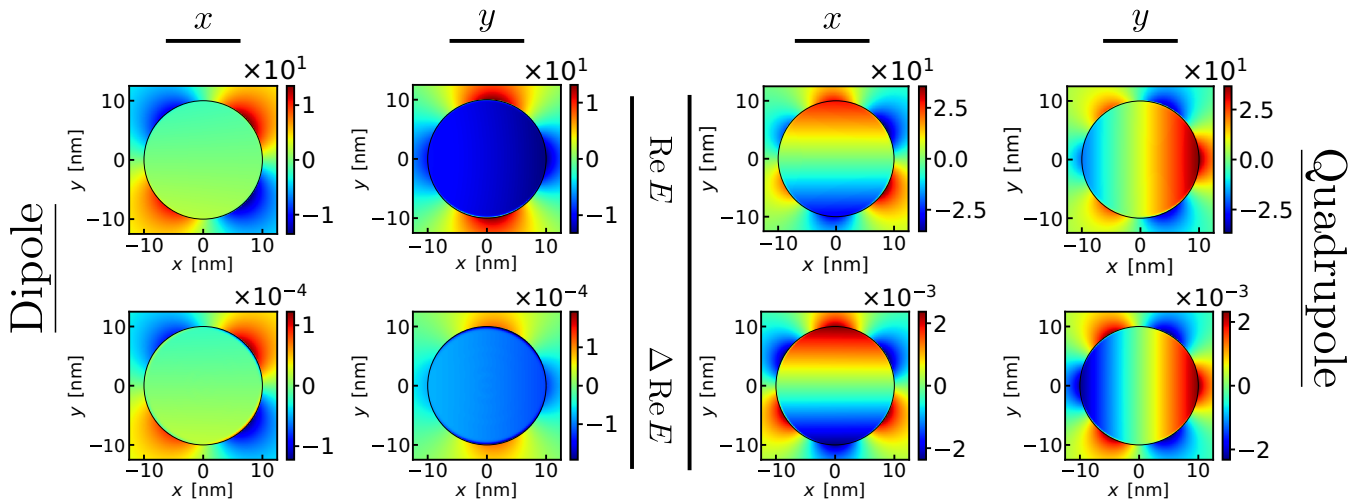

FIG. 7. Illustration of the electric field distributions of dipolar (left panel) and quadrupolar (right panel) resonances within the Halevi model (upper row) as well as their relative differences to the corresponding modal distributions for the high-frequency Euler-Drude model (lower row). The difference has been normalized to the maximum value obtained with the Euler-Drude model at the respective frequency. Positive (negative) values of the respective distribution are complemented by positive (negative) values in the relative difference. The maximum enhancement reaches about a tenth of a permille at the dipole frequency and about two permille at the quadrupole frequency. The relative difference inside the scatterer is more inhomogeneous for the quadrupolar mode.

To complement the spectral investigations, we have employed the ADE technique to adopt the Halevi model for time-domain simulations. The additional dispersion of the latter yields a modification of the diffusion current of Fick type. We have shown that the propagation of the induced charge, related to the current modifications, shares similarities with a hybrid, diffusive-wavelike paradigm as described by the Cattaneo equation. The origin of the current has further been rooted to the viscoelastic shear.

We have completed our analytical analysis by comparing the Halevi model to the GNOR model—the latter being another extension of the Euler-Drude model that includes a diffusive contribution to the current, however, without asymptotic comparison to a semiclassical model. The GNOR-model features several differences to the Halevi model that include a low-frequency, characteristic velocity exceeding the Thomas-Fermi value and the deviation from the Euler-Drude model for frequencies beyond the volume plasma frequency. Further, we have shown that the GNOR-model is connected to a difference in the scaling of the diffusive lengthscale at plasmonic frequencies by an additional factor ω_p/γ relative to the Halevi model. For typical metals and assuming a frequency-independent GNOR-diffusion constant this additional factor takes on values $\omega_p/\gamma \sim 10^2..10^3$. As a result, while in the GNOR model the diffusive length exceeds the length scale of combined compression and shear, the opposite case is manifest in the Halevi model. Finally, we have shown that a direct comparison between the GNOR and the Halevi model at intermediate frequencies suggest that the GNOR-diffusion constant is complex valued and frequency dependent.

Employing a time-domain formulation of the Halevi model, we have numerically determined the spatiotemporal evolution of the electric field's distributions in and around silver nanowires. We have found that under pulsed excitations, the differences of the electric field components between the Halevi and the Euler-Drude model take on the form of wave packets. These buildup at the subsurface region, subsequently propagate towards the cylinder center from where they spread across the entire cross section of the cylinder and eventually fade away. This behavior correlates with a concomitant oscillatory contribution of the diffusive current. Upon analyzing the resulting wave packet envelopes, we have inferred an estimate of the corresponding group velocity, which, in fact, has turned out to be smaller than all natural scales of the Halevi and viscoelastic model. Further, we have determined a positive chirp of the wave packets spatial frequencies towards the center of the cylinder. Performing an on-the-fly Fourier transform of the temporal evolution of the field distribution we have determined the mode distributions of the dipolar and quadrupolar resonance. The Halevi model preserves the respective symmetries of the Euler-Drude model and—at least for monomers—the differences between both models are rather small.

Based on our results a few comments regarding possible future routes are in order. First of all, our results concerning scatterers rely on the hard-wall boundary condition in the form of the so-called slip boundary condition. On the mesoscopic scale, this constraint could be lifted by introducing an infinitesimal charge sheet, e.g., via a variation of the composite-surface model of Ref. [75]. On the one hand, this would yield an approximate treatment of spill-out effects that are presently not contained within our model. On the other hand, this could phenomenologically account for "chemical interface damping", i.e., charge-transfer effects across the surface of a plasmonic nanoparticle and its surrounding host material [27]. This could be further compared to the theory of Persson [61] that connects the latter to interactions with resonance states of adsorbates that form at a metal surface. All these suggestions further rely on a spatially constant equilibrium charge density. Lifting this constraint yields, in

particular, another account of spill-out effects [17]. It is also interesting to investigate to which extent the inhomogeneous equilibrium density can be associated with spatially inhomogeneous material parameters (e.g., the shear modulus). In elastic theory, such a characteristic effect is associated with a mixture of transverse and longitudinal waves. In such a description, we expect the mixture to occur deeper within the scatterer as compared to the hard-wall-boundary scenario with constant equilibrium density. This should also have an impact on the nonlocal bulk resonances. In addition, a detailed discussion on the difference between slip- and no-slip boundary conditions is highly desirable. The latter cannot be enforced *ad hoc*, but has to be physically motivated with regard to the specific surface characteristics of the scatterer under consideration [54]. A potential justification could be inferred by embedding the Halevi model into the viscoelastic model, which, in turn, would provide a clear path to the introduction of transverse nonlocality. Specifically, the absence of a tangential surface current due to e.g. surface irregularities can affect the neighborhood of the surface due to shear, thus providing a physical motivation of the no-slip model. So far, the latter has been considered only for a half-space of metal yielding a nonlocal correction to the well-known s-polarized Fresnel formula [39]. Further, an application of the full viscoelastic model to thin semiconductor films has been performed in Ref. [60], albeit with the slip boundary condition.

Finally, for the setup of a single nanowire considered in our paper, the relative differences in the widths and amplitudes of resonances between the Halevi and Euler-Drude model have turned out to be small. However, this does not always have to be the case. It is, therefore, very interesting to seek for physical setups in which changes to the optical, dielectric bulk properties (as encoded in the dielectric functions) are more pronounced. For instance, in Ref. [28] it has been pointed out that the extinction of colloidal metallic nanospheres is very sensitive to the changes of bulk quantities. Further, it is interesting to investigate dimer and related structures, i.e., to consider the effect of the Halevi model on the electromagnetic field distribution in nanogap systems. Recently, such systems have witnessed significant attention due to the potential of strongly modified light-matter interaction, for instance, with regards to strong coupling of emitters as well as quantum [76,77] and/or enhanced nonlinear optical effects. Finally, more complex geometries offering additional geometric parameters will be highly relevant in order to tune the near-field modifications brought about by the Halevi model. For completeness, we should like to note that the implementation of the Halevi model for fully three-dimensional systems is straightforward.

ACKNOWLEDGMENTS

G.W., F.I., and K.B. acknowledge funding by the German Research Foundation (DFG) in the framework of the Collaborative Research Center 1375 “Nonlinear Optics down to Atomic Scales (NOA)” (Project No. 398816777). N.A.M. is a VILLUM Investigator supported by VILLUM FONDEN (Grant No. 16498) and the Danish National Research Foundation (Project No. DNRF165). The authors wish to thank Matthias Plock for fruitful discussions.

APPENDIX A: QUASISTATIC CYLINDRICAL PLASMON-POLARITON RESONANCES

In this Appendix, we calculate the plasmon-polariton resonances localized at the surface of the cylinder within the quasistatic approximation and the Halevi model [see Eq. (23)].

In Sec. III, we have considered the scattering of a plane wave that propagates in vacuum and is normally incident onto an infinitely extended circular cylinder for the polarization perpendicular to the cylinder axis. Via Ruppin’s extension of the corresponding Mie solution (expansion into cylindrical harmonics), we have obtained the expansion coefficients of the scattered field in Eq. (16). The surface resonances can be determined from the poles of expansion coefficients according to

$$0 = [c_n + D_n(k_\mathrm{T}a)]H_n(k_0a) - \sqrt{\epsilon_\mathrm{T}(\omega)}H_n'(k_0a). \tag{A1}$$

From the definitions of the three wave numbers k_0, k_L, k_T evaluated close to the surface plasma frequency ω_sp, we deduce for cylinders with radii smaller than half the plasma wavelength c/ω_p and larger than half the effective extent of nonlocality $\beta_\mathrm{HF}/\omega_\mathrm{p}$ (about 10 nm and 0.01 nm, respectively, for common metals) that

$$|k_0a|,\ |k_\mathrm{T}a| \ll 1 \ \text{ and } \ 1 \ll |k_\mathrm{L}a|. \tag{A2}$$

Accordingly, we may utilize of Eq. (A1) the Bessel functions’ asymptotic representations (see Ref. [55]). We then find the implicit dispersion relation

$$\epsilon_\mathrm{T}(\omega) = -\frac{1 - in/k_\mathrm{L}a}{1 + in/k_\mathrm{L}a} \approx -1 + \frac{2in}{k_\mathrm{L}a}, \tag{A3}$$

where, in the last step, we have further assumed that $n \ll |k_\mathrm{L}a|$. Using Eq. (10), we find that the local solution to first order in γ/ω_p assumes the form

$$\omega_\mathrm{loc} = \omega_\mathrm{sp} - \frac{i\gamma}{2} + \mathcal{O}\left(\frac{\gamma^2}{\omega_\mathrm{sp}^2}\right). \tag{A4}$$

Here, we have selected the solution with a positive real part. The resulting dispersion relation resembles that of the local surface plasmons at a planar interface between vacuum and a half-space filled with metal. Consequently, for normally incident and quasistatic electric fields polarized perpendicular to the cylinder axis, the geometry does not alter the local surface plasmons. This is a consequence of the quasistatic approximation. Otherwise, even the local solution would depend on the pole order n and radius a.

Next, we seek a solution to Eq. (A3) that includes a nonlocal correction to Eq. (A4) to leading order. Therefore, we use the Ansatz

$$\omega_n = \omega_\mathrm{sp}\left(1 - \frac{i\gamma}{2\omega_\mathrm{sp}} + \delta_n\right) \ \text{ with } \ |\delta_n| \ll 1. \tag{A5}$$

Considering the Taylor expansion in δ_n of Eq. (10) around $\omega = \omega_n$, we find

$$\epsilon_\mathrm{T}(\omega_n) = \epsilon_\mathrm{T}(\tilde{\omega}_\mathrm{sp}) + \epsilon_\mathrm{T}'(\tilde{\omega}_\mathrm{sp})\omega_\mathrm{sp}\delta_n + \mathcal{O}\left(\delta_n^2\right), \tag{A6}$$

where we have introduced $\tilde{\omega}_{\rm sp} = \omega_{\rm sp} - i\gamma/2$. To make further progress, we require the following Taylor expansions in $\gamma/\omega_{\rm sp}$,

$$\epsilon_{\rm T}(\tilde{\omega}_{\rm sp}) = -1 + \mathcal{O}\left(\frac{\gamma^2}{\omega_{\rm sp}^2}\right),$$
$$\epsilon'_{\rm T}(\tilde{\omega}_{\rm sp}) = \frac{4}{\omega_{\rm sp}} + \mathcal{O}\left(\frac{\gamma^2}{\omega_{\rm sp}^2}\right), \tag{A7}$$

which yields

$$\epsilon_{\rm T}(\omega_n) \approx -1 + 4\delta_n. \tag{A8}$$

Equating this result with the r.h.s. of Eq. (A3), we find for the nonlocal correction the implicit relation

$$\delta_n = \frac{in}{2a}\frac{1}{k_{\rm L}(\omega_n)}. \tag{A9}$$

Keeping Eq. (20) in mind, we have to expand Eq. (4) in a manner analogous to Eqs. (A6) and (A7) and eventually arrive at

$$\beta_{\rm H}^2(\omega_n) \approx \left[1 - \frac{4i}{9}\frac{\gamma}{\omega_{\rm sp}}\right]\beta_{\rm HF}^2. \tag{A10}$$

Here, we have dropped the first-order term of the Taylor expansion because this is proportional to $(\gamma/\omega_{\rm sp})\delta_n$.

Upon inserting Eqs. (A8) and (A10) into Eq. (20) we obtain

$$\frac{1}{k_{\rm L}(\omega_n)} \approx -\frac{i\beta_{\rm HF}}{\omega_{\rm sp}}\left[1 - \frac{2i}{9}\frac{\gamma}{\omega_{\rm sp}} + \delta_n\right], \tag{A11}$$

which, when inserted into Eq. (A9), gives

$$\delta_n = \frac{n\beta_{\rm HF}}{2\omega_{\rm sp}a}\left(1 - \frac{2i}{9}\frac{\gamma}{\omega_{\rm sp}}\right)\left[1 - \frac{n\beta_{\rm HF}}{2\omega_{\rm sp}a}\right]^{-1}. \tag{A12}$$

Indeed, since $n \ll \omega_{\rm sp}a/\beta_{\rm HF}$ and $\gamma \ll \omega_{\rm sp}$, we find $|\delta_n| \ll 1$. To first order in $n\beta_{\rm HF}/\omega_{\rm sp}a$, the second term inside the square brackets can be neglected and this gives Eq. (23).

APPENDIX B: CONVERGENCE STUDY

We have assessed and ascertained the accuracy of our simulations performed in Sec. VI with reference to the extinction efficiency. The numerical results are obtained by computing the Poynting vector, which is integrated along the (inside and outside of the) TF/SF contour and normalized by the incident irradiance as well as twice the cylinder radius. The cylinder ($a = 10$ nm) is centered in a square TF/SF contour of 40 nm edge length. To prevent unphysical back reflections, we placed a PML far away, resulting in a SF-region bounded by a 440 × 440 nm outer square padded from the outside by a 300 − nm thick PML. Thus, the Silver-Müller boundary condition is also placed far away (see Fig. 8). Since (in the chosen frequency range) the nonlocal effects are significant close to the surface of the cylinder we have identified the surface discretization as the most crucial parameter. In our convergence study, employing GMSH [73] as meshing software, we have constrained the maximum edge length of the triangular finite elements in the cylinder to about 1 nm and have constructed a sequence of meshes with consecutively smaller edge lengths at the boundary down to about 0.2 nm. Away from the cylinder boundary the edge length slowly increases (see Fig. 8). In particular, we employed five different meshes with optimal edge length at the surface $h_{\rm surf}$ defined as $\{0.6; 0.5; 0.4; 0.3; 0.2\}$ nm. This led to minimal in-sphere radii of $\{0.12; 0.10; 0.08; 0.06; 0.04\}$ nm. Employing, e.g., the Halevi model, in each simulation, the surface dipole and quadrupole frequency converged to the analytical values of $\omega \approx 0.684\omega_{\rm p}$ and $\omega \approx 0.708\omega_{\rm p}$. However, there was a finite difference in the amplitude of the extinction efficiency when comparing the simulations and Mie theory. Hence, we have considered the frequency-dependent relative difference

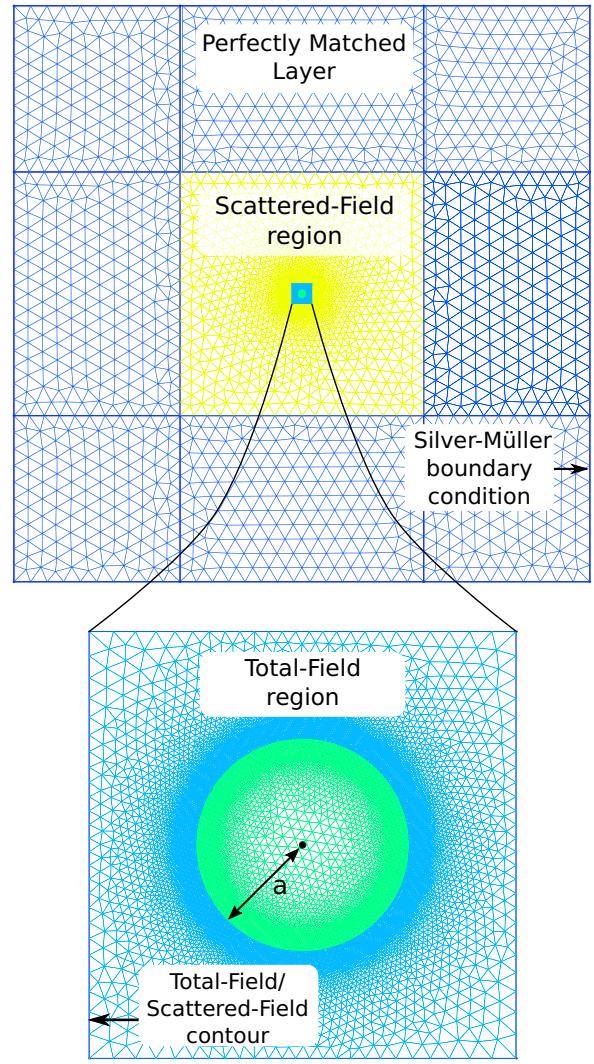

FIG. 8. A representation of the meshed computational domain (see Sec. VI) and a zoom into the TF region including the cylindrical scatterer. Notice the progressive refinement of the mesh cells at the boundary of the cylinder.

$$\Delta Q_{\rm rel}(\omega) = \frac{\left|Q_{\rm ext}^{\rm Num}(\omega) - Q_{\rm ext}^{\rm Mie}(\omega)\right|}{Q_{\rm ext}^{\rm Mie}(\omega)}, \tag{B1}$$

where "Num" and "Mie" refer to the numerical and analytical efficiency, respectively. Applying this measure, averaged over the relevant frequency interval of $\omega \in (0.6, 0.8)\omega_{\rm p}$, to

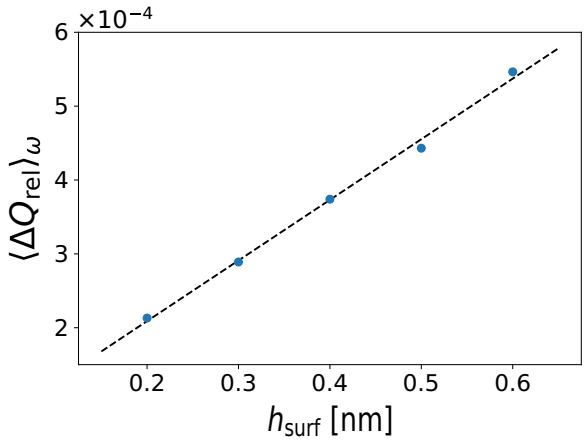

FIG. 9. Convergence study for the time-domain simulation yielding the evolution of the auxiliary current as depicted in Fig. 5. The study is based on Eq. (B1) averaged over the relevant frequency range of $\omega \in (0.6, 0.8)\omega_p$. The analytical reference is obtained from the Mie theory outlined in Sec. III.

each edge discretization, a converging trend can be observed in Fig. 9. Further, evaluated at the quadrupolar resonance frequency, Eq. (B1) amounted to relative deviations below one percent for the coarser and around one permille for the finest mesh. Similarly, applying the measure at the dipolar frequency, the deviation was always well below one permille.

Eventually, we opted for the finest simulation as depicted in Fig. 8. Note that the actually resolved spatial distance is even smaller than the in-sphere radius of 0.04 nm, being given by the interspacing of nodes inside each triangle. This value is smaller than the Thomas-Fermi length $\sim v_F/\omega_p \approx 0.1$ nm of silver, which is the characteristic lengthscale for the metallic nonlocal effects considered here. The maximum in-sphere radius of the cylinder equals roughly 0.32 nm.

APPENDIX C: COMPUTATIONAL RESOURCES

In Sec. VI we have considered the temporal evolution of the electric field inside a silver nanowire excited by a normally incident plane wave with electric field polarized within the horizontal plane. We have associated an oscillatory contribution prevalent within the field employing the Halevi model but absent when enforcing the linear hydrodynamic material model with the auxiliary current discussed in Sec. IV. For the simulation of both models, we have employed the mesh depicted in Fig. 8. When applying the DGTD method we used the same time step for the temporal integration on all mesh elements. Due to stability requirements, the finest triangle then limits this global time step from above [66]. We opt for a physical time step of $dt \approx 1.27$ as. The total physical simulation time amounts to 127 fs, allowing to not only study the above mentioned oscillation but also for a converged extinction spectrum obtained from an on-the-fly Fourier transform. The simulation of the Halevi model (yielding the current evolution displayed in parts in Fig. 5) has been performed on a desktop PC providing up to 32GB RAM using eight cores on an INTEL XEON E-2288G CPU and took about 4 days and 7 hours. About 70 percent of the time was devoted to temporal integration, leaving about 30 percent of the time for saving data and performing the Fourier transformation. In essence, these run times originate from the small time step that result from the need to faithfully represent the curved geometry via finite elements with sufficiently small edge length. Here, curvilinear finite elements [78] would provide a much better representation of the geometry, thereby considerably reducing the required computational resources.

[1] Q. Zhang, X. Cai, X. Yu, S. Carregal-Romero, W. J. Parak, R. Sachan, Y. Cai, N. Wang, Y. Zhu, and D. Y. Lei, Electron energy-loss spectroscopy of spatial nonlocality and quantum tunneling effects in the bright and dark plasmon modes of gold nanosphere dimers, Adv. Quantum Technol. **1**, 1800016 (2018).

[2] T. Itoh, Y. S. Yamamoto, Y. Kitahama, and J. Balachandran, One-dimensional plasmonic hotspots located between silver nanowire dimers evaluated by surface-enhanced resonance Raman scattering, Phys. Rev. B **95**, 115441 (2017).

[3] M. Rothe, Y. Zhao, J. Müller, G. Kewes, C. T. Koch, Y. Lu, and O. Benson, Self-assembly of plasmonic nanoantenna–waveguide structures for subdiffractional chiral sensing, ACS Nano **15**, 351 (2021).

[4] A. Wiener, H. Duan, M. Bosman, A. P. Horsfield, J. B. Pendry, J. K. W. Yang, S. A. Maier, and A. I. Fernández-Domínguez, Electron-energy loss study of nonlocal effects in connected plasmonic nanoprisms, ACS Nano **7**, 6287 (2013).

[5] A. Sundaramurthy, K. B. Crozier, G. S. Kino, D. P. Fromm, P. J. Schuck, and W. E. Moerner, Field enhancement and gap-dependent resonance in a system of two opposing tip-to-tip Au nanotriangles, Phys. Rev. B **72**, 165409 (2005).

[6] G. W. Bryant, F. J. García de Abajo, and J. Aizpurua, Mapping the plasmon resonances of metallic nanoantennas, Nano Lett. **8**, 631 (2008).

[7] E. Zaremba, Surface-plasmon dispersion for diffuse boundary scattering, Phys. Rev. B **9**, 1277 (1974).

[8] G. Wegner and C. Henkel, Remarks about surface plasmons and their stability, arXiv:2005.03716.

[9] C. David and F. J. García de Abajo, Surface plasmon dependence on the electron density profile at metal surfaces, ACS Nano **8**, 9558 (2014).

[10] C. Ciracì, E. Poutrina, M. Scalora, and D. R. Smith, Origin of second-harmonic generation enhancement in optical split-ring resonators, Phys. Rev. B **85**, 201403(R) (2012).

[11] C. Ciracì, E. Poutrina, M. Scalora, and D. R. Smith, Second-harmonic generation in metallic nanoparticles: Clarification of the role of the surface, Phys. Rev. B **86**, 115451 (2012).

[12] D.-N. Huynh, M. Moeferdt, C. Matyssek, C. Wolff, and K. Busch, Ultrafast three-wave-mixing in plasmonic nanostructures, Appl. Phys. B **122**, 139 (2016).

[13] K. R. Hiremath, L. Zschiedrich, and F. Schmidt, Numerical solution of nonlocal hydrodynamic Drude model for arbitrary

shaped nano-plasmonic structures using Nédélec finite elements, J. Comput. Phys. **231**, 5890 (2012).
[14] M. Moeferdt, T. Kiel, T. Sproll, F. Intravaia, and K. Busch, Plasmonic modes in nanowire dimers: A study based on the hydrodynamic Drude model including nonlocal and nonlinear effects, Phys. Rev. B **97**, 075431 (2018).
[15] N. A. Mortensen, Mesoscopic electrodynamics at metal surfaces—From quantum-corrected hydrodynamics to microscopic surface-response formalism, Nanophotonics **10**, 2563 (2021).
[16] R. Ruppin, Extinction properties of thin metallic nanowires, Opt. Commun. **190**, 205 (2001).
[17] G. Toscano, J. Straubel, A. Kwiatkowski, C. Rockstuhl, F. Evers, H. Xu, N. A. Mortensen, and M. Wubs, Resonance shifts and spill-out effects in self-consistent hydrodynamic nanoplasmonics, Nat. Commun. **6**, 7132 (2015).
[18] N. A. Mortensen, S. Raza, M. Wubs, T. Søndergaard, and S. I. Bozhevolnyi, A generalized non-local optical response theory for plasmonic nanostructures, Nat. Commun. **5**, 3809 (2014).
[19] S. Raza, S. I. Bozhevolnyi, M. Wubs, and N. A. Mortensen, Nonlocal optical response in metallic nanostructures, J. Phys.: Condens. Matter **27**, 183204 (2015).
[20] P. Halevi, Hydrodynamic model for the degenerate free-electron gas: Generalization to arbitrary frequencies, Phys. Rev. B **51**, 7497 (1995).
[21] N. D. Mermin, Lindhard Dielectric function in the relaxation-time approximation, Phys. Rev. B **1**, 2362 (1970).
[22] C. R. Martin, Nanomaterials: A membrane-based synthetic approach, Science **266**, 1961 (1994).
[23] M. I. Stockman, Nanofocusing of Optical Energy in Tapered Plasmonic Waveguides, Phys. Rev. Lett. **93**, 137404 (2004).
[24] R. M. Dickson and L. A. Lyon, Unidirectional plasmon propagation in metallic nanowires, J. Phys. Chem. B **104**, 6095 (2000).
[25] I. Villó-Pérez and N. R. Arista, Hydrodynamical model for bulk and surface plasmons in cylindrical wires, Surf. Sci. **603**, 1 (2009).
[26] S. Conti and G. Vignale, Elasticity of an electron liquid, Phys. Rev. B **60**, 7966 (1999).
[27] H. Hövel, S. Fritz, A. Hilger, U. Kreibig, and M. Vollmer, Width of cluster plasmon resonances: Bulk dielectric functions and chemical interface damping, Phys. Rev. B **48**, 18178 (1993).
[28] U. Kreibig and C. von Fragstein, The limitation of electron mean free path in small silver particles, Z. Phys. **224**, 307 (1969).
[29] A. Compte and R. Metzler, The generalized Cattaneo equation for the description of anomalous transport processes, J. Phys. A: Math. Gen. **30**, 7277 (1997).
[30] S. C. Ying, Hydrodynamic response of inhomogeneous metallic systems, Nuov. Cim. B **23**, 270 (1974).
[31] I. Tokatly and O. Pankratov, Hydrodynamic theory of an electron gas, Phys. Rev. B **60**, 15550 (1999).
[32] G. C. Aers, B. V. Paranjape, and A. D. Boardman, Non-radiative surface plasma-polariton modes of inhomogeneous metal circular cylinders, J. Phys. F: Met. Phys. **10**, 53 (1980).
[33] F. Bloch, Bremsvermögen von Atomen mit mehreren Elektronen, Z. Phys. **81**, 363 (1933).
[34] F. Haas, *Quantum Plasmas: An Hydrodynamic Approach* (Springer, New York, 2011).
[35] M. Ancona, Hydrodynamic models of semiconductor electron transport at high fields, VLSI Design **3**, 101 (1995).
[36] C. L. Gardner, The quantum hydrodynamic model for semiconductor devices, SIAM J. Appl. Math. **54**, 409 (1994).
[37] Z. A. Moldabekov, M. Bonitz, and T. S. Ramazanov, Theoretical foundations of quantum hydrodynamics for plasmas, Phys. Plasmas **25**, 031903 (2018).
[38] W. Yan, Hydrodynamic theory for quantum plasmonics: Linear-response dynamics of the inhomogeneous electron gas, Phys. Rev. B **91**, 115416 (2015).
[39] M. Hannemann, G. Wegner, and C. Henkel, No-slip boundary conditions for electron hydrodynamics and the thermal Casimir pressure, Universe **7**, 108 (2021).
[40] L. Landau and E. Lifshitz, *Fluid Mechanics, Course of Theoretical Physics*, 2nd ed. (Elsevier Science, Oxford, 2013), Vol. 6.
[41] G. Giuliani and G. Vignale, *Quantum Theory of the Electron Liquid* (Cambridge University Press, Cambridge, 2005).
[42] B. Bertini, F. H. L. Essler, and E. Granet, Bogoliubov-Born-Green-Kirkwood-Yvon Hierarchy and Generalized Hydrodynamics, Phys. Rev. Lett. **128**, 190401 (2022).
[43] C. Kittel, *Quantum Theory of Solids*, 2nd revised ed. (Wiley, New York, 1963).
[44] N. Ashcroft and N. Mermin, *Solid State Physics* (Holt, Rinehart, and Winston, New York, 1976).
[45] F. Della Sala, Orbital-free methods for plasmonics: Linear response, J. Chem. Phys. **157**, 104101 (2022).
[46] C. Wolff, R. Rodríguez-Oliveros, and K. Busch, Simple magneto–optic transition metal models for time–domain simulations, Opt. Express **21**, 12022 (2013).
[47] J. Lindhard, On the properties of a gas of charged particles, Mat. Fys. Medd. K. Dan. Vidensk. Selsk. **28**, 1 (1954).
[48] G. G. Stokes, in *Mathematical and Physical Papers Cambridge Library Collection - Mathematics* (Cambridge University Press, Cambridge, 2009), Vol. 1, pp. 75–129.
[49] P. Morse and H. Feshbach, *Methods of Theoretical Physics. Part 1* (McGraw-Hill, New York, 1953).
[50] L. Landau and Lifshitz, *Theory of Elasticity*, *Course of Theoretical Physics*, 2nd ed. (Pergamon Press, Oxford, 1970).
[51] F. Flores and F. García-Moliner, Classical electrodynamics of non-specular conducting surfaces, J. Phys. France **38**, 863 (1977).
[52] C. Bohren and D. Huffman, *Absorption and Scattering of Light by Small Particles* (Wiley, New York, 2008).
[53] A. R. Melnyk and M. J. Harrison, Theory of optical excitation of plasmons in metals, Phys. Rev. B **2**, 835 (1970).
[54] S. Raza, G. Toscano, A.-P. Jauho, M. Wubs, and N. A. Mortensen, Unusual resonances in nanoplasmonic structures due to nonlocal response, Phys. Rev. B **84**, 121412(R) (2011).
[55] M. Abramowitz and I. A. Stegun, *Handbook of Mathematical Functions with Formulas, Graphs, and Mathematical Tables* (Dover, New York, 1964).
[56] S. Maier, *Plasmonics: Fundamentals and Applications* (Springer, New York, 2007).
[57] P. B. Johnson and R. W. Christy, Optical constants of the noble metals, Phys. Rev. B **6**, 4370 (1972).
[58] R. Gross and A. Marx, *Festkörperphysik* (De Gruyter, München, 2018).
[59] P. Jewsbury, Electrodynamic boundary conditions at metal interfaces, J. Phys. F: Met. Phys. **11**, 195 (1981).

[60] D. de Ceglia, M. Scalora, M. Vincenti, S. Campione, K. Kelley, E. Runnerstrom, J.-P. Maria, G. Keeler, and T. Luk, Viscoelastic optical nonlocality of doped-cadmium-oxide epsilon-near-zero thin films, Sci. Rep. **8**, 9335 (2018).

[61] B. Persson, Polarizability of small spherical metal particles: Influence of the matrix environment, Surf. Sci. **281**, 153 (1993).

[62] T. Christensen, W. Yan, S. Raza, A.-P. Jauho, N. A. Mortensen, and M. Wubs, Nonlocal response of metallic nanospheres probed by light, electrons, and atoms, ACS Nano **8**, 1745 (2014).

[63] M. K. Svendsen, C. Wolff, A.-P. Jauho, N. A. Mortensen, and C. Tserkezis, Role of diffusive surface scattering in nonlocal plasmonics, J. Phys.: Condens. Matter **32**, 395702 (2020).

[64] T. Christensen, W. Yan, A.-P. Jauho, M. Soljačić, and N. A. Mortensen, Quantum Corrections in Nanoplasmonics: Shape, Scale, and Material, Phys. Rev. Lett. **118**, 157402 (2017).

[65] A. V. Uskov, I. E. Protsenko, N. A. Mortensen, and E. P. O'Reilly, Broadening of plasmonic resonance due to electron collisions with nanoparticle boundary: A quantum mechanical consideration, Plasmonics **9**, 185 (2014).

[66] K. Busch, M. König, and J. Niegemann, Discontinuous Galerkin methods in nanophotonics, Laser Photonics Rev. **5**, 773 (2011).

[67] M. Chester, Second Sound in Solids, Phys. Rev. **131**, 2013 (1963).

[68] S. Bozhevolnyi, L. Martin-Moreno, and F. Garcia-Vidal, *Quantum Plasmonics* (Springer International Publishing, Berlin, 2016).

[69] J. L. Warren and R. A. Ferrell, Nonlocal current-field relationship in metals, Phys. Rev. **117**, 1252 (1960).

[70] J. Hesthaven and T. Warburton, *Nodal Discontinuous Galerkin Methods: Algorithms, Analysis, and Applications* (Springer, New York, 2007).

[71] J. Niegemann, R. Diehl, and K. Busch, Efficient low-storage Runge–Kutta schemes with optimized stability regions, J. Comput. Phys. **231**, 364 (2012).

[72] A. Hille, M. Moeferdt, C. Wolff, C. Matyssek, R. Rodríguez-Oliveros, C. Prohm, J. Niegemann, S. Grafström, L. M. Eng, and K. Busch, Second harmonic generation from metal nanoparticle resonators: Numerical analysis on the basis of the hydrodynamic Drude model, J. Phys. Chem. C **120**, 1163 (2016).

[73] C. Geuzaine and J.-F. Remacle, Gmsh: A 3-D finite element mesh generator with built-in pre- and post-processing facilities, Int. J. Numer. Meth. Engng. **79**, 1309 (2009).

[74] Y. Yang, A signal theoretic approach for envelope analysis of real-valued signals, IEEE Access **5**, 5623 (2017).

[75] B. Horovitz and C. Henkel, Surface plasmons at composite surfaces with diffusive charges, Europhys. Lett. **97**, 57010 (2012).

[76] D. Reiche, M. Oelschläger, K. Busch, and F. Intravaia, Extended hydrodynamic description for nonequilibrium atom-surface interactions, J. Opt. Soc. Am. B **36**, C52 (2019).

[77] D. Reiche, F. Intravaia, and K. Busch, Wading through the void: Exploring quantum friction and nonequilibrium fluctuations, APL Photonics **7**, 030902 (2022).

[78] J. Viquerant, and C. Scheid, A 3D curvilinear discontinuous Galerkin time-domain solver for nanoscale light-matter interactions, J. Comput. Appl. Math. **289**, 37 (2015).